# Reassessment of the radiative width of the Hoyle state from gamma ray spectroscopy using OSCAR

by

Wanja Paulsen

Thesis

for the degree of

Master of Science


Faculty of Mathematics and Natural Sciences
University of Oslo

August 10, 2020

# Abstract

The Hoyle state is an extraordinary resonant state in Carbon-12 and a prime example of how remarkable the nature of our universe truly is. It is famous not only for the prediction of its existence in 1953[1] by one of the pioneers of nuclear astrophysics, Fred Hoyle, but also for its key role in the production of atomic nuclei in stars. The aim of this thesis is to measure the probability of successfully creating stable Carbon-12 by gamma decay from the Hoyle state to the ground state of Carbon-12. In stars Carbon-12 is made from fusion of three alpha-particles in what is called the 'triple-alpha process', a nucleosynthesis process happening inside stars.

The probability of gamma decaying from this resonant state was investigated by populating the Hoyle state in Carbon-12 through the $^{12}\mathrm{C}(p, p'\gamma\gamma)$-reaction with protons of 10.7 MeV at the Oslo Cyclotron Laboratory, using the $LaBr_3$ array OSCAR and the silicon-strip particle detector SiRi[2]. The goal was to reach the Hoyle state where the triple-alpha process produces Carbon-12 and measure proton-gamma-gamma coincidences, meaning the amount of nuclei decaying back into stable Carbon-12 by gamma decay. Today the determined probability of decaying to stable Carbon-12 from the Hoyle state is $\approx 0.06\%$[3] while $\approx 99.94\%$[3] of Carbon-12 nuclei will split into three alpha-particles.

Using the gamma decay branching ratio, the radiative branching ratio of the Hoyle state was determined to be $\Gamma_{rad}/\Gamma = 7.08(85) \times 10^{-4}$ and the radiative width of the Hoyle state was determined to be $\Gamma_{rad} = 6.6(6) \times 10^{-3}$ eV. The previously adopted value for the radiative branching ratio from eight measurements performed between 1961 and 1976[4, 5, 6, 7, 8, 9, 10] is $\Gamma_{rad}/\Gamma = 4.13(11) \times 10^{-4}$[3]. The measurement from this thesis is 72% larger than this adopted value. A measurement performed in 2014 by T. Kibédi *et al.* determined the radiative branching ratio of the Hoyle state to be $\Gamma_{rad}/\Gamma = 6.69(6) \times 10^{-4}$[11], this value is 68% larger than the adopted value.

The measurement of the radiative branching ratio of the Hoyle state from this thesis supports the measurement performed by T. Kibédi *et al.* Based on the results from this thesis, further investigation of the radiative branching ratio of the Hoyle state is suggested. A new experiment to measure the gamma decay branching ratio has been proposed, where the experiment will be optimised for the use of OSCAR and SiRi. Furthermore, a study of the consequences of a larger value for the rate of the triple-alpha process in astronomical models is suggested, as this will impact subsequent nucleosynthesis processes as well as the lifetime of stars.

## Thank you

To my main supervisor Sunniva Siem, you have not only been my supervisor during this thesis, you have helped me build confidence in myself and my abilities to an extent I did not know I was capable of. Your encouragement and belief in students are truly some of your greatest strengths. I will always be grateful for everything you have done for me.

To my co-supervisor Tomas K. Eriksen, without your endless patience and help the results of this thesis would never have been finished. Through your guidance during this thesis, I have experienced how science is a journey of highs and lows, and I aspire to have the knowledge and scientific creativity you possess.

The past years at the Nuclear physics group at the University of Oslo have been filled with laughter, kindness, and amazing experiences I will forever remember with a smile. Not only have I been able to partake and learn from nuclear physics experiments in Orsay, Cape Town, Bucharest, and Southern Japan, I have also experienced swimming in the arctic ocean of Svalbard, climbing mountains in South Africa, and biking in the countryside of Hyogo. All of these experiences were shared with my friends and colleagues, whom I hope to share experiences with for many more years.

## Takk

Hallooo Cecilie! Vår tid sammen i Fysikkbygningen er fylt av gode minner fra forelesninger i FYS3110, kattesokker, Ganni, den fineste diamant, fisketurer ved trappa i Vestfløyen og så mye mer. Om ti år skal jeg se tilbake å le og gråte av våre sprø påfunn og savne disse årene, mens jeg synger på 'Lover' av Taylor Swift. Du er en inspirasjon og gjør meg til en bedre versjon av meg selv, takk.

Julie, jeg kommer aldri til å glemme den fortapte øyjenta som møtte deg første dag på Blindern. Du tok meg imot med åpne armer og hjalp meg å finne og akseptere hvem jeg var, og er. Jeg hadde aldri vært den personen jeg er i dag uten deg. Takk for alt det fine og vanskelige som har vært, og alt som skal komme.

Kjære Kevin, du har vært der for meg gjennom alt. Jeg kunne ikke gjort dette uten deg og dine gode, varme klemmer. Du står alltid opp for meg og heier på meg og min karriere. Du betyr alt for meg.

Til slutt vil jeg takke familien min for deres endeløse støtte i mitt plutselige, sprøe påfunn for seks år siden: Å satse alt på at jeg ville klare dette. Det hadde ikke gått uten Mamma, Rhea og ikke minst Chantel.

*Wanja Paulsen*

August 10, 2020

# Contents

# Chapter 1

# Introduction

We humans are carbon-based, oxygen-breathing lifeforms whose life and existence is continuously sustained by our star, the sun. 'We are made of starstuff' is a well-known quote from the famous astronomer Carl Sagan[12], which is absolutely true. The universe is filled with giant cauldrons of creation, processes which are finely tuned by nature. Nucleosynthesis, the process of creating heavier nuclei from lighter nuclei, happens not only in our own sun but in all kinds of stars, even the dead remnants of stars can produce atomic nuclei.

Carbon-12 is the fourth most abundant isotope existing in our universe and is produced at several different astronomical sites. The process behind the creation of Carbon-12 is an example of a fine-tuned parameter of nature. Carbon-12 has a remarkable production process but it is most famous for its resonant property, an excited quantum state by the name of the Hoyle state. The existence, properties and relevance of the Hoyle state and the series of fine-tuned resonances in the nucleosynthesis processes following the production route of carbon has been discussed by many physisicts[13, 14, 15, 3]. The interest goes beyond the physics of nature, even as having a more philosophical or religious meaning, often mentioned as supporting the anthropic principle[1]. There are in other words many motives behind the research of the creation and purpose of Carbon-12, but in this thesis the motivation is to understand the nature of the Hoyle state and the nuclear properties of this quantum state.

The Hoyle state and its nuclear properties have been studied in various ways and methods since its prediction[1] and the experimental evidence of its existence in 1953[16]. The process starts with the fusion of two helium nuclei, which creates the unstable isotope Beryllium-8. A third helium nucleus fuses together with the unstable Beryllium-8 to create Carbon-12. The probability of the superposition of three helium nuclei to successfully become stable Carbon-12 is of utmost importance

[1]In short the anthropic principle discusses how scientific observation of the universe would not be possible if the laws of the nature had been incompatible with the development of sentient life. As described by Freer and Fynbo 'The principle relies on the fact that intelligent life exists, to assert certain properties of the universe must exist, i.e. we exist therefore so must the [Hoyle state]'[3].

for several branches of astronomy and nuclear astrophysics, for example astrophysical calculations of elemental abundances and stellar evolution.

The lifespan of a star is also directly related to the production rate of Carbon-12. This is because the rate of the triple-alpha process decides the amount of time the star will burn helium through this process. This rate is given as

$$r_{3\alpha} = \Gamma_{rad} \exp\left(-Q_{3\alpha}/kT\right), \tag{1.1}$$

where $\Gamma_{rad}$ is the electromagnetic radiative width of the Hoyle state, $Q_{3\alpha}$ is the energy released in the alpha-decay leading back to to $^{8}$Be and $T$ is the stellar temperature[11]. If the triple-alpha reaction rate increases or decreases, the lifetime of the star will decrease or increase, respectively. This is because the density of helium inside will decrease faster if the probability of fusion is higher. Since the reaction rate depends directly on the width of the Hoyle state, the function describing the probabilities of the different decay paths, astrophysical calculations are very sensitive to its value and precision. Therefore, it is important to know this quantity precisely. In this thesis the radiative branching ratio and the radiative width of the Hoyle state will be determined by measuring the gamma decay branching ratio of this resonant state.

This radiative decay branching ratio, or the radiative width, has been measured several times before, with the first measurement performed in 1961[4]. This measurement focused on the gamma-decay branch from the Hoyle state, which is the decay-branch of highest probability. A total of 9 measurements of this decay-branch has been done between 1961 and 2014[4, 5, 6, 7, 8, 9, 10]. All yielded quite similar results except the result from the measurement performed in 2014[11].

The experiment performed by T. Kibédi *et al.*[11] in 2014 was performed using the same method as Obst *et al.*[10] used in 1976 to measure the gamma decay branching ratio of the Hoyle state. The difference was the increased number of NaI-detectors from four to twenty-eight, as well as the use of SiRi[2] as the particle telescope. The experiment was performed at The Oslo Cyclotron Laboratory using the NaI-scintillation array CACTUS and the particle telescope SiRi as a proton-gamma-gamma coincidence measurement. The analysis resulted in a radiative branching ratio $\Gamma_\gamma/\Gamma$ which is 68% higher than the adopted value from earlier measurements. So far no explanation has been established to explain why T. Kibédi[11] found such a surprising value for the radiative branching ratio.

The purpose of this thesis work is to do a measurement of the gamma decay branching ratio of the Hoyle state in Carbon-12 and use this measurement to calculate the radiative branching ratio and the radiative width. These result will be be compared to the adopted value from previous measurements[4, 5, 6, 7, 8, 9, 10] as well as the surprising result from T. Kibédi[11]. There is a need to confirm whether or not a similar experiment will yield a measurement of the gamma decay branching ratio which is comparable to T. Kibédi[11]. Not only because of the effects of an increased radiative branching ratio has on the rate of the triple-alpha process and continued nucleosynthesis beyond Carbon-12, but because the OCL has newly

updated experimental equipment. The $LaBr_3$ scintillation array OSCAR has better energy resolution, better time resolution which causes less random coincidences and is closer to the target chamber, compared to the former NaI scintillation array CACTUS. In the data analysis of the measurement using CACTUS it was not possible to distinguish the gamma decay from the Hoyle state and the double escape peak of the 4.44 MeV gamma decay from the first excited state in Carbon-12. With OSCAR this is not a problem anymore and the 3.21 MeV gamma ray from the Hoyle state will be possible to detect.

chapter 2 will give the reader an introduction to the concept of nucleosynthesis, with an emphasis on the helium-burning phase. The role of Carbon-12 in this process is briefly been touched upon in this introduction to nucleosynthesis, but a more in-depth explanation of the triple-alpha process and the Hoyle state will be given later in the chapter. A thorough description as to how this elusive resonance can be measured experimentally is given in section 2.6 as well as the results of earlier measurements of this measurement in section 2.9. In chapter 3 the experimental equipment and set-up used in this thesis is described, in addition to section 3.2 describing the nuclear reaction used. Calibration of data is also shown in section 3.3.

The analysis of the data collected during the experiment is explained in chapter 4. The final measurement of the gamma decay branching ratio, the radiative branching ratio and the radiative width as well as discussion about the results and comparison to previous measurements are presented in chapter 5. Finally a summary and future outlook are presented in chapter 6 and chapter 7.

# Chapter 2

# The Hoyle state and the 3$\alpha$-process

This chapter gives an introduction to stellar nucleosynthesis, describes the theory behind the triple-alpha process and the Hoyle state, as well as their roles in the nucleosynthesis process of a star. A look into whom first explained the triple-alpha process and the mathematical problems of this description will also be explained, as well as the explanation for these problems found by the physicist Fred Hoyle. How the gamma decay path from the Hoyle state can be measured experimentally is explained, along with a presentation of the previous measurements performed on this state since its initial discovery.

## 2.1 Stellar nucleosynthesis

The light and heat emitted from a star originates from the fusion of atomic nuclei as elements are being created inside the star through thermonuclear reactions. The process releases enormous amounts of energy mainly in the form of gamma rays and thermal heat, the light and the heat the Earth is sustained by. The star is fusing lighter elements to create heavier elements, a process called stellar nucleosynthesis. The starting point of this process is always the fusion of hydrogen, while the end point varies depending on the stars mass and temperature. Stars which are over 8 times the size of our sun will for a brief period of time be able to fuse iron[17].

When a star has fused enough of the nuclei possible with the current temperature of the star, the radiation pressure outwards will decrease and the gravitational pressure will make the star enter a collapsing phase. In this collapsing phase the temperature of the star will increase, increasing the probability of fusing heavier elements together. This self-governing mechanism continues until the probability for fusion becomes so low that the gravitational collapse results in the star becoming a degenerate star, supernovae or even a black hole. Ejection of the matter created in a star happens in several ways and is one of the essential reasons that the Earth and other planets exists. The most efficient and energetic method is the supernovae, where further fusion of elements can happen while matter is explosively ejected from

the star.

There are several processes and astronomical environments where nucleosynthesis, the creation of atomic nuclei, can take place. These processes occur through different reaction mechanisms and on different time scales. All stars use thermonuclear reactions to create atomic nuclei, but they can have different nucleosynthesis processes during their lifetime, or even after their initial death. This depends on the stars location in the Hertzsprung-Russel diagram[17, p.9], a method of classifying stars based on their temperature, mass and luminosity. The thermonuclear reactions inside stars are primarily the fusion of lighter nuclei to heavier nuclei, the process responsible for the production of elements from hydrogen to iron and nickel. The most common thermonuclear reaction besides fusion is the **s-process** or **slow neutron capture-process**[17, p.505]. Initially the process starts with a single seed nucleus, which over thousands of years can absorb a neutron and either decay back, become a heavier istope or a different element based on the lifetime of the current nucleus. How heavy the seed nucleus becomes depends on the amount of time it is situated in an environment where the s-process is possible. The s-process is believed to be responsible for approximately half of all isotopes heavier than iron and mainly the stable isotopes[17, p.505].

Another process utilising neutron-capture is the **r-process** or the **rapid neutron capture process**[17, p.522][18]. The difference between the s-process and the r-process is that the r-process happens in the matter of seconds with tens or hundreds of neutrons captured in succession per nucleus, such that the seed cannot decay closer to stability before the next neutron-capture. This means that the seed nucleus will go from a medium mass to a heavy or even super-heavy mass nucleus within a very short amount of time, creating heavy and very exotic isotopes which have never been observed. These heavy exotic nuclei will instantly decay into the heaviest stable isotopes we have found so far in the nuclear chart. The astrophysical environments which is recently observed to be a r-process site are neutron star mergers such as GW170817[19, 18, 20]. There are also processes which consists of reactions based on $(p,\gamma)$-reactions and $(\gamma,n)$-reactions such as the **p-process** and the **rp-process**[17, p.542]. The creation of atomic nuclei is a complex set of processes and these are just three of the several processes which are known to be responsible for nucleosynthesis of atomic nuclei in the universe.

## 2.2 Helium burning in stars

From their initial creation stars are continuously producing atomic nuclei through the process of nucleosynthesis. This continues for millions of years until the moment when fusion is no longer energetically possible, when the star will begin its phase of death. The stars lifespan can be categorized into different periods of nucleosynthesis, starting with the period of hydrogen burning. Over time the density of hydrogen will decrease and the density of helium will increase, the star enters the collapsing

phase. In this phase the equilibrium between the stars radiation pressure outwards and the gravitational force inwards is lost, and the gravitational force will overcome the radiation pressure. The pressure of the gravitational force on the star will make the star contract, which increases the temperature of the stars core, making fusion of heavier elements possible[21]. This is when the triple-alpha process becomes possible, and through the Hoyle state of $^{12}$C, eventually the Carbon-Nitrogen-Oxygen-cycle and helium burning including continuation of the triple-alpha process will occur in the star.

The helium burning phase in stars is responsible for the production of $^{8}$Be, $^{12}$C, $^{16}$O and $^{20}$Ne through a series of remarkable coincidences. It starts with the fusion of two helium nuclei to form $^{8}$Be. $^{8}$Be has an incredibly short life-time, but the large abundance of helium creates a constant equilibrium concentration of beryllium available for fusion to happen. Within the short amount of time a beryllium nucleus exists, a third helium nucleus fuses together with $^{8}$Be. The sum of these three helium nuclei have a Q-value of $Q = -7366.59(4)$ keV[22], being very close to the energy of the Hoyle state, a resonant state in $^{12}$C[16, 1] at 7.65 MeV, making it possible to create $^{12}$C from $^{8}$Be. This superposition of nuclei can decay electromagnetically from the Hoyle state and become stable $^{12}$C. The focus of this thesis is to calculate the radiative branching ratio as well as the radiative width of this Hoyle state in $^{12}$C by measuring this electromagnetic decay. This fusion of three helium nuclei is called the triple-alpha process, a process which has very low probability of success. The low probability originates from the fact that the Hoyle state is above the alpha break-up threshold, therefore decaying mainly by alpha emission. The triple-alpha process is also the only method of creating $^{12}$C from lighter elements, thus being a critical bottleneck in the nucleosynthesis of element[23].

The following fusion processes after the initial creation of Carbon-12 are part of the Carbon-Nitrogen-Oxygen-cycle or the CNO-cycle, a catalytic cycle including several different cycles producing isotopes in the mass region between Carbon and Oxygen[17, p.369] as well as being a second source of hydrogen and helium production in the star[17, p.369]. If $^{12}$C undergoes fusion with another helium nucleus, $^{16}$O is created. The energy window this combination is within has no resonant state, in fact this region has a 7.12 MeV $1^-$-state[15, p.410], making this process much less probable because of the nuclear property of isospin selection rules. This means that the probability of creating $^{16}$O from $^{12}$C is lower than the probability to create $^{12}$C from $^{8}$Be. The result is therefore a high abundance of Carbon-12 even if there is a massive abundance of Helium-4 available for fusion with the Carbon-12 nuclei inside the stars environment. The next step in the chain of nucleosynthesis is fusion between $^{16}$O and $^{4}$H, creating $^{20}$Ne. This process is hindered by the nuclear property of parity conservation rules, meaning that newly produced $^{16}$O-nucleus will not instantly become $^{20}$Ne. This allows a concentration of $^{16}$O to build up inside the star. One could speculate as to what our universe would look like if the resonance in $^{12}$C and nuclear properties hindering the production of $^{16}$O and $^{20}$Ne did not exist. The

elemental abundance of our universe would be completely different, as well as stars having significantly shorter lives. This series of resonances is the major reason why the Hoyle state is the subject of philosophical and religious discussion regarding the anthropic principle or the existence of a divine being[3, 13, 14, 15].

In the very early age of the galaxy supernovae were the main source of distribution of Carbon-12 into the universe[1]. This was because more massive stars capable of returning Carbon-12 into the interstellar medium of the universe had yet not evolved[13]. The production of Carbon-12 was inside the stars core and at later stages, in the adjoining layers of more massive stars. At the present age of our galaxy, the production site of Carbon-12 through the triple-alpha process is mainly in thermal pulses in shells of AGB stars at the end of their hydrogen burning stage[13], stars which are in the asymptotic branch of star-categorization. The Hoyle state and the triple-alpha process are principal to the creation of Carbon-12 in all astronomical environments.

## 2.3 The triple-alpha process

In the beginning of both the helium-burning phase and the CNO-cycle the triple-alpha process plays an important role, the triple-alpha process is the only method of producing elements beyond the point of $^8$Be, the result of fusing two helium nuclei together. Because of this the triple-alpha process is often called a 'bottle-neck process', meaning that this process is one of the slowest processes in the nucleosynthesis of atomic nuclei inside stars. The width of this process controls how much and how fast the subsequent processes happen.

The triple-alpha process is a two-step process originally explained by Hans Bethe[24] as being highly improbable because it required temperatures 50 times higher than what was known at the time[24, 3]. The next physicists who tried to explain the problems related to the temperature and this process was E. E. Salpeter[25] and E. J. Öpik[26] in 1952. The reaction can be described as

$$^4\mathrm{He} + {}^4\mathrm{He} \rightleftharpoons {}^8\mathrm{Be} \tag{2.1}$$

$$^8\mathrm{Be} + {}^4\mathrm{He} \rightleftharpoons {}^{12}\mathrm{C} + \gamma \tag{2.2}$$

or in a more condensed notation,

$$3 \times {}^4\mathrm{He} \rightleftharpoons {}^{12}\mathrm{C}^* \rightarrow {}^{12}\mathrm{C} + 7.65\mathrm{MeV}. \tag{2.3}$$

The half-life of $^8$Be is $T_{1/2} = 8.19 \times 10^{-17}$s[27], but only a kinetic energy of $\mathrm{E}_\alpha = 95 \pm 5$ keV relative to the stars temperature is needed for its formation, making

[1]Stars of our present galaxy often have heavier materials from supernovas of past stars available. The order of processes presented here are more representative of stars in the early universe, where matter ejected from stars had not yet reached the interstellar medium[13].

approximately a fraction 1 to $10^9$ of the stars material $^8$Be at all times[23]. Before the beryllium nucleus can decay back into two helium nuclei, a fusion reaction with a third alpha particle must happen in order to form $^{12}$C. The third alpha particle must undergo fusion with the beryllium nucleus before it is split, and the combined kinetic energy of the superposition of the three alpha-particles must match a resonant state in $^{12}$C, namely the Hoyle state[1]. This superposition of three alpha-particle must be close to 0.3193 MeV, luckily this is the approximate temperature inside red giant stars[1].

The explanation of this process was initially seen as problematic because the conversion rate of three alpha-particles to $^{12}$C versus the destruction rate would be too low to explain the abundance of carbon[1]. In 1953 a man named Fred Hoyle wrote a paper showing how resonances in nuclei can contribute greatly to the abundance of specific nuclei and how the triple-alpha process happens at a much lower temperature than the rest of the CNO-cycle does[1]. Through this he was able to solve the $^{12}$C abundance problems that E. E Salpeter and E. J. Öpik had in their calculations. It was also here he formally presented the resonance in $^{12}$C which is known as the Hoyle state today. The properties of this resonant state which is the topic of this thesis will be explained in the following section.

## 2.4 The Hoyle state

Fred Hoyle was a pioneer in the field of astrophysics and also one of the authors of one of the most famous scientific papers in history, namely the B$^2$FH-paper[23] written by M. Burbigde, G. Burbigde, A. Fowler and Fred Hoyle in 1957. This article, originally named 'The synthesis of elements in stars' was a scientific landmark in the field of nuclear astrophysics as well as astrophysics, as it contained theoretical explanations of stellar nucleosynthesis supported by astronomical and laboratory data. From its publication and until today it has been highly influential in both astronomy and nuclear physics.

In 1953 Fred Hoyle made a remarkable prediction regarding the triple-alpha process and the creation of Carbon-12 in an article describing the importance of resonances in nucleosynthesis processes between carbon and nickel[1]. He was also well-aware of the theoretical calculations and the abundance problems behind the triple-alpha process by E. E. Salpeter[25] and E. J. Öpik[26]. Based on the problems behind these calculations and his studies into the possibility of resonances boosting isotopic abundances, he presented his famous prediction: There must be a resonant state in Carbon-12 and the energy of this resonant state had to be around 7.68 MeV. Not only that, he argued that this state had to be a $J^\pi = 0^+$ so that the alpha particles were not hindered by the centrifugal barrier in the potential of the scattering system. This would solve the abundance-problems behind the theoretical calculations of the triple-alpha process[1].

The same year Wenzel *et al.* published a paper where they had experimentally

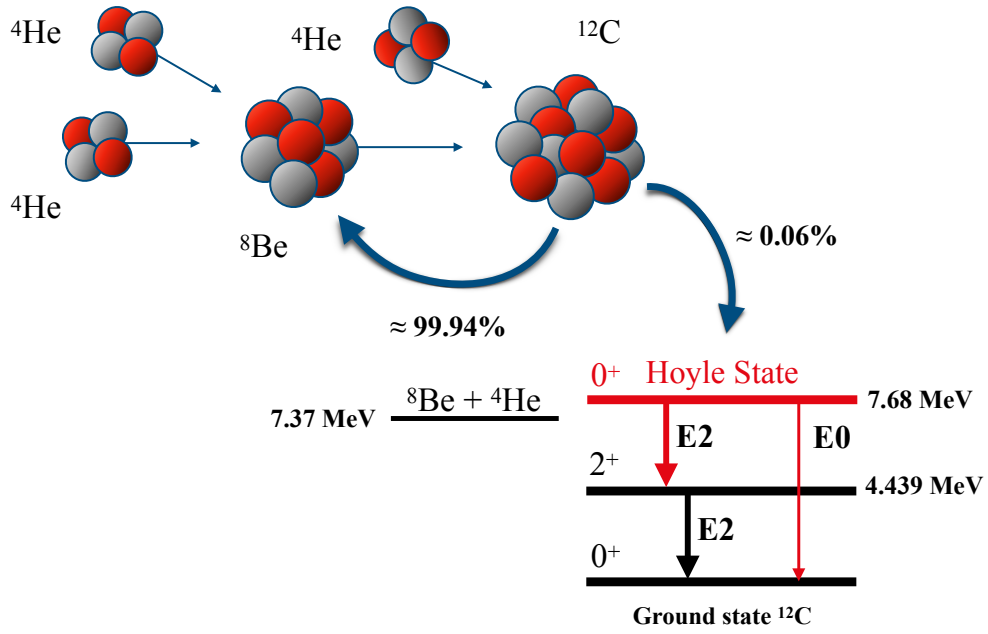


**Figure 2.1:** Illustration showing the triple-alpha process and the consecutive decay from the Hoyle state to the ground state in $^{12}$C. The probabilities presented are current known values[3].

confirmed this resonant state at an energy of 7.65 MeV in $^{12}$C[16] using a $^{14}$N(d, $\alpha$)$^{12}$C reaction. This measurement was performed to test Hoyle's prediction. It was for this reason and several other important contributions as a pioneer in the field of nuclear astrophysics that this resonant state in $^{12}$C was named the Hoyle state after Fred Hoyle. Quoted from the Wenzel *et al.* paper: 'We are indebted to Professor Hoyle for pointing out to us the astrophysical significance of this level'[16].

In Figure 2.1 an illustration of the triple-alpha process and the Hoyle state, as well as all non-negligible decay paths this superposition of three helium nuclei can decay through is presented. Only $\approx 0.06\%$ successful superpositions of helium will decay to the ground state in $^{12}$C[28, 3]. As visible in the illustration, the Hoyle state is a spinless s-wave resonance, just above the alpha-particle decay threshold in $^{12}$C at 7.37 MeV[3].

The radiative decay from the Hoyle state occurs mainly by two different decay paths, as seen in Figure 2.1. Either a two-step gamma cascade consisting of E2-transitions through the first excited $2^+$ state at 4.44 MeV or through a pair decay E0-transition directly to the ground state. Only these two decay paths are non-negligible because the Hoyle state is a $J^\pi = 0^+$ state. To reach the ground state of the same $J^\pi = 0^+$ there can be no angular momentum transfer if the transition is

direct and therefore not by gamma decay. The two-step gamma cascade accounts for most of the radiative decay from the Hoyle state and consists of a 3.215 MeV E2-transition to the $J^\pi = 2^+$ first excited state followed by a 4.44 MeV E2-transition to the $J^\pi = 0^+$ ground state.

## 2.5 The radiative width of the Hoyle state

When three helium nuclei fuse together through the triple-alpha process, their combined energy can possibly be in energy range of the Hoyle state around 7.65 MeV. The superposition of those three nuclei have several decay paths to proceed through, where some are negligible. The probability of decay is commonly described in terms of 'decay width', where the total decay width of a state is the sum of 'partial widths' describing each of the probabilities available. The total width of the Hoyle state can be written as

$$\Gamma = \Gamma_\alpha + \Gamma_\gamma + \Gamma_\pi + \Gamma_{\mathrm{CE}}, \tag{2.4}$$

a sum of the decay width of $\alpha$-break up $\Gamma_\alpha$, gamma decay to the 4.44 MeV $2^+$ state $\Gamma_\gamma$, pair production $\Gamma_\pi$ and internal conversion $\Gamma_{\mathrm{CE}}$. The decay width describing the internal conversion electrons are negligible as seen in Table 2.1.

This total width is useful when you want to know the probability of each decay path, for example how probable it is for the triple-alpha process to decay back into an alpha particle and a $^8$Be nucleus. A very useful quantity is the probability of the triple-alpha process to successfully produce Carbon-12, this is defined by the last three terms that decay to the ground state of Carbon-12 in Equation 2.4. This radiative width can be written as

$$\Gamma_{rad} = \Gamma_\gamma^{\mathrm{E2}} + \Gamma_\pi^{\mathrm{E0}} + \Gamma_\pi^{\mathrm{E2}} + \Gamma_{\mathrm{CE}}^{\mathrm{E0}} + \Gamma_{\mathrm{CE}}^{\mathrm{E2}}. \tag{2.5}$$

The radiative width is the sum of the width for decaying by gamma-emission $\Gamma_\gamma^{\mathrm{E2}}$ to the first excited state through an E2-transition, pair-production $\Gamma_\pi^{\mathrm{E0}}$ to the ground state through an E0-transition or $\Gamma_\pi^{\mathrm{E2}}$ to the first excited state through an E2-transition and lastly an internal conversion $\Gamma_{\mathrm{CE}}^{\mathrm{E0}}$ to the ground state through an E0-transition or $\Gamma_{\mathrm{CE}}^{\mathrm{E2}}$ to the first excited state through an E2-transition. The current values for the decay paths and their widths can be seen in Table 2.1. The current known value for the total width of the Hoyle state is $\Gamma = 9.3(3)$ eV[3] and for the alpha-break up the width is $\Gamma_\alpha = \Gamma - \Gamma_{rad} \approx 9.29$ eV. The known radiative width is equal to $\Gamma_{rad} = 6.4(8) \times 10^{-3}$ eV[3] or a total of 0.06% probability to successfully decay to the ground state of $^{12}$C.

Observing and measuring the widths of the different decay paths in Equation 2.5 experimentally can be very challenging. The probability of the triple-alpha process to produce Carbon-12 successfully is incredibly low, requiring large amounts of statistics.

| Decay type | E0-transition | E2-transition |
|---|---|---|
| $\gamma$-decay | | 98.4% |
| Pair production | 1.5% | $\leq 0.09\%$ |
| Internal conversion | $\leq 0.01\%$ | $\leq 0.01\%$ |

**Table 2.1:** Table showing the calculated values for the probability of the different decay-paths from the Hoyle state to the ground state in the radiative width of the Hoyle state as seen in Equation 2.5[11, 29].

Because it is hard to observe each term individually the radiative width has previously been deduced experimentally using the equation[10]

$$\Gamma_{rad} = \left[\frac{\Gamma_{rad}}{\Gamma}\right] \times \left[\frac{\Gamma}{\Gamma_{\pi}^{\mathrm{E0}}}\right] \times \left[\Gamma_{\pi}^{\mathrm{E0}}\right]. \tag{2.6}$$

Here $\Gamma$ is the total width of the Hoyle state as given in Equation 2.4, $\Gamma_{rad}$ is the radiative width as given in Equation 2.5 and $\Gamma_{\pi}^{\mathrm{E0}}$ is the absolute E0 decay width. $\Gamma_{\pi}^{\mathrm{E2}}$, $\Gamma_{\mathrm{CE}}^{\mathrm{E2}}$ and $\Gamma_{\mathrm{CE}}^{\mathrm{E0}}$ are excluded because the magnitude of these widths are negligible as seen in Table 2.1. The term $\Gamma_{rad}/\Gamma$ can be approximated as

$$\frac{\Gamma_{rad}}{\Gamma} = \frac{\Gamma_{\gamma}^{\mathrm{E2}} \times (1 + \alpha_{tot})}{\Gamma} + \frac{\Gamma_{\pi}^{\mathrm{E0}}}{\Gamma}, \tag{2.7}$$

where $\alpha_{tot}$ is the theoretical total E2 conversion coefficient and $\Gamma_{\pi}^{\mathrm{E0}}/\Gamma$ is the pair decay branching ratio. The absolute E0 decay width $\Gamma_{\pi}^{\mathrm{E0}}$ can be measured directly[3] and the E0 pair decay branching ratio has been measured several times[3] with the most recent measurement performed by T. K. Eriksen *et al.* at Australian National University[30] with improved precision compared to previous measurements.

## 2.6 Measuring the gamma-decay branching ratio

The gamma decay branch $\Gamma_{\gamma}^{\mathrm{E2}}$ is the width of largest contribution to the radiative width of the Hoyle state in Equation 2.5. This gamma cascade decays through an E2-transition to the first excited state at 4.44 MeV and then proceeds to the ground state through another E2-transition. Measuring this transition is the objective of this thesis and can be done using the equation

$$\left(\frac{\Gamma_{\gamma}^{\mathrm{E2}}}{\Gamma}\right)^{7.65} = \frac{N_{020}^{7.65}}{N_{\mathrm{singles}}^{7.65} \times \epsilon_{3.21} \times W_{020}^{7.65} \times \epsilon_{4.44}}. \tag{2.8}$$

This equation can be used to calculate the gamma decay branching ratio of the Hoyle state using particle-gamma-gamma coincidences. Here $N_{020}^{7.65}$ is the net coincidence yield, in other words, the number of particles that were measured in coincidence with the 3.22 MeV and 4.44 MeV gamma cascade de-exciting the Hoyle state[10]. $N_{\text{singles}}^{7.65}$ is the total number of particles populating the Hoyle state including the particles that yielded gamma-gamma coincidences. $\epsilon_{3.21}$ is the absolute photopeak efficiency of the 3.21 MeV gamma ray from the Hoyle state to the first excited state at 4.44 MeV. $\epsilon_{4.44}$ is the absolute photopeak efficiency for the 4.44 MeV gamma ray from the first excited state to the ground state in $^{12}$C. $W_{020}^{7.65}$ is the angular correlation correction term, as described in Equation 2.10.

To reduce the uncertainty of Equation 2.8 and increase the precision of the measurement, a rewritten equation of the form

$$\left(\frac{\Gamma_{\gamma}^{\text{E2}}}{\Gamma}\right)^{7.65} = \left(\sum_{\theta=0}^{180} \frac{N_{020}^{7.65}(\theta)}{C_{\theta} \times W_{020}^{7.65}(\theta)}\right) \frac{1}{K} \times \frac{1}{N_{\text{singles}}^{7.65} \times \epsilon_{3.21}/M \times \epsilon_{4.44}/M} \tag{2.9}$$

will be used. Here $\theta$ sums over the different angle combinations between the two detectors in the proton-gamma-gamma coincidences, $C_{\theta}$ is the number of detector combinations in OSCAR for the angle $\theta$ and $M = 30$ is the number of detectors in OSCAR. $W_{020}^{7.65}(\theta)$ is the angular correlation correction term at the angle $\theta$. The variable $K$ is the number of terms in the sum, as this method of calculation will calculate a gamma decay branching ratio at each angle $\theta$. Including the term $1/K$ will therefore calculate the average value for the gamma decay branching ratio. The term $N_{020}^{7.65}(\theta)$ is the term $N_{020}^{7.65}$ depending on the angle $\theta$. The term $N_{020}^{7.65}(\theta)$ will consist of a single peak after adjusting the data using the sum in Equation 2.9, removing the issue of low statistics at each angle. The consequence of having low statistics for the proton-gamma-gamma coincidences means that calculation of the area of this peak becomes less precise, increasing the uncertainty of the measurement. Ideally the efficiency terms $\epsilon_{3.21}$ and $\epsilon_{4.44}$ should be used to adjust the data during sorting and the efficiency of each detector of OSCAR should be known. During this thesis there was no source measurement performed, therefore an average value for the efficiency of each detector was chosen. In subsection 4.2.3 a description of how the efficiency was measured is presented.

The angular correlation term $W_{020}^{7.65}$ describes the angular dependency of the emission of gamma rays in the cascade from the 7.65 MeV $0^+$ Hoyle state and the 4.44 MeV $2^+$ state. This angular correlation term is the most difficult quantity to obtain in Equation 2.8 because of the low yield of particle-gamma-gamma coincidences. The gamma cascade from the Hoyle state is a $0^+ \rightarrow 2^+ \rightarrow 0^+$ transition. The 3.21 MeV gamma ray emitted from the $0^+$ Hoyle state at 7.65 MeV is emitted with an isotropic angular distribution, however this gamma ray produces a certain spin orientation of the $2^+$ state, this results in a non-isotropic distribution of the 4.44 MeV gamma ray , creating an angular correlation between the two gamma rays. The angular correla-

tion correction between two gamma rays in a $0^+ \rightarrow 2^+ \rightarrow 0^+$ cascade can be written as[10]

$$W_{020}(\theta) = A_0 P_0(\cos\theta) + A_2 P_2(\cos\theta) + A_4 P_4(\cos\theta),$$
$$P_0 = 1, \qquad P_2 = \frac{1}{2}\left(3\cos^2\theta - 1\right), \quad P_4 = \frac{1}{8}\left(35\cos^4\theta - 30\cos^2\theta + 3\right), \tag{2.10}$$

where $\theta$ is the angle between two detectors, $P_0$, $P_2$, $P_4$ are Legendre polynomials and $A_0$, $A_2$, $A_4$ are values fitted to the data. This $W_{020}(\theta)$ has to be calculated for all possible angles $\theta$ between all detectors used in the measurement.

## 2.7 Alternative solution for the angular correlation correction

An alternative method to measure the gamma decay branching ratio of the Hoyle state is to eliminate the dependency of an angular correlation correction $W_{020}$ in Equation 2.8 by utilizing the angular correlation of a $0^+ \rightarrow 2^+ \rightarrow 0^+$ cascade from a state in $^{28}$Si, which is similar to the gamma-cascade from the Hoyle state. This method was used by Obst *et al.* in their measurement of the gamma decay branching ratio in 1976[10]. In Figure 2.2 level schemes with selected levels for $^{12}$C and $^{28}$Si are shown. The gamma transitions marked in red is the initial gamma decay of the two cascades which are similar. The gamma-cascades have the same type of $0^+ \rightarrow 2^+ \rightarrow 0^+$-transition, as well as the first gamma ray having almost identical energy. The very useful property of this 4.98 MeV state in $^{28}$Si is that the gamma decay intensity is equal to $I_\gamma(\mathrm{E2}) = 0.9983$(see section 2.8) which is approximately equal to one. This means that the gamma decay branching ratio is approximately equal to one. We can write this gamma decay branching ratio on the same form as the branching ratio for the Hoyle state in Equation 2.8 so that

$$\left(\frac{\Gamma_\gamma^{\mathrm{E2}}}{\Gamma}\right)^{4.98} = \frac{N_{020}^{4.98}}{N_{\mathrm{singles}}^{4.98} \times \epsilon_{1.78} \times W_{020}^{4.98} \times \epsilon_{3.20}} = 1. \tag{2.11}$$

Here the $N_{020}^{4.98}$ is the net particle-gamma-gamma coincidence yield, $N_{\mathrm{singles}}^{4.98}$ is the yield of particle-gamma-gamma coincidences, $\epsilon_{3.20}$ is the absolute photopeak efficiency of the first gamma ray, $\epsilon_{1.78}$ is the absolute photopeak efficiency of the second gamma ray and $W_{020}^{4.98}$ is the angular correlation of the second gamma ray with respect the first gamma ray. Because it is equal to one, we can implement the equation into the radiative gamma-decay branching ratio for the Hoyle state, as given in Equation 2.9. This is done by dividing Equation 2.9 by Equation 2.11, this combined equation becomes

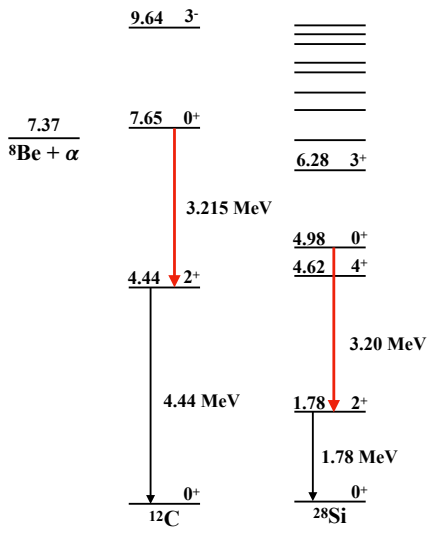


**Figure 2.2:** Illustration comparing the level scheme for $^{12}$C and $^{28}$Si, highlighting the comparable gamma transitions in red and the following gamma transitions in black. The break-up threshold for the triple-alpha process is also shown. The figure is inspired by Figure 1 in Obst *et al.*[10].

$$\left(\frac{\Gamma_\gamma}{\Gamma}\right)^{7.65} = \frac{N_{020}^{7.65}}{N_{020}^{4.98}} \times \frac{N_{\text{singles}}^{4.98}}{N_{\text{singles}}^{7.65}} \times \frac{\epsilon_{1.78}}{\epsilon_{4.44}} \times \frac{\epsilon_{3.20}}{\epsilon_{3.21}} \times \frac{W_{020}^{4.98}}{W_{020}^{7.65}}. \tag{2.12}$$

The advantage of this combined equation is in the last two terms. Firstly, the ratio of absolute photopeak efficiency $\epsilon_{3.20}/\epsilon_{3.21} \approx 1.0$ therefore there is no need to measure this efficiency. Secondly and also the biggest advantage is the cancellation of the angular correlation coefficients from the term $W_{020}^{4.98}/W_{020}^{7.65} \approx 1.0$. By implementing the gamma-decay branching ratio of the 4.98 MeV $0^+$ state in $^{28}$Si the potential problem with low statistics in the angular distribution is removed. In addition to the particle-gamma-gamma coincidence and proton singles measurements of $^{12}$C and $^{28}$Si, only the photopeak efficiencies of the 1.78 MeV and 4.44 MeV are needed to deduce the gamma decay branching ratio of the Hoyle state.

## 2.8 Efficiency calculations

The absolute photopeak efficiency describes the efficiency of a detector to detect a gamma ray emitted by a source. It is defined as the ratio of the number of counts recorded by the detector to the number of gamma rays emitted by the source in all

directions, this can be written as

$$\frac{N_{\text{detected}}}{N_{\text{emitted}}}. \tag{2.13}$$

In this thesis the detector set-up used has 57% of $4\pi$-angle coverage around the source[31], making the detection efficiency as high as possible. As the calculation of the gamma decay branching ratio of the Hoyle state will be performed directly using Equation 2.9 and Equation 2.12, the absolute photopeak efficiency is needed at the four energies $\epsilon_{1.78}$, $\epsilon_{3.20}$, $\epsilon_{3.21}$ and $\epsilon_{4.44}$. The absolute photopeak efficiency is usually determined using a radioactive source of known activity, emitting gamma rays in the energy range where the efficiency is needed. This method makes it possible to use Equation 2.13 directly. In this thesis an approximation to this method was used, where the ratio between particles populating the excited states at the needed energies and the particle-gamma coincidences was used as input to Equation 2.13. This is possible because the 4.44 MeV $2^+$ state, 4.98 MeV $0^+$ and 1.78 MeV $2^+$ states in $^{12}$C and $^{28}$Si respectively have a radiative width equal to one and decay through E2 gamma ray transitions mainly.

To show that this is indeed possible we can calculate this for all the required states. Beginning with the 4.98 MeV $0^+$ state in $^{28}$Si, the branching ratio is

$$\left(\frac{\Gamma_{rad}}{\Gamma}\right)^{4.98} = I_\pi(\text{E0}) + I_K(\text{E0}) + I_\gamma(\text{E2}) + I_\pi(\text{E2}) + I_K(\text{E2}) = 1, \tag{2.14}$$

where the intensities for decay through pair creation are presented by $I_\pi(\text{E0})$, $I_\pi(\text{E2})$, K-shell electron capture intensities presented by $I_K(\text{E0})$, $I_K(\text{E2})$ and gamma decay intensities is presented by $I_\gamma(\text{E2})$. Here we can express $I_K(\text{E0})$ and $I_\pi(\text{E0})$ such that

$$I_K(\text{E0}) = q_k^2(\text{E0/E2})\alpha_K(\text{E2})I_\gamma(\text{E2}), \qquad I_\pi(\text{E0}) = I_K(\text{E0})\frac{\Omega_\pi(\text{E0})}{\Omega_K(\text{E0})}, \tag{2.15}$$

where $q_K^2(\text{E0/E2})$ is the ratio between E0 and E2 K-shell electron capture transitions, $\alpha_K(\text{E2}) = I_K/I_\gamma$ is the conversion coefficient for E2-transitions from the K-shell and $\alpha_\pi(\text{E2})$ is the conversion coefficient for internal pair formation. The contribution from further shells such as $\alpha_L(\text{E2})$ are of the order of $10^{-9}$ and was therefore omitted in all calculations[32]. $\Omega_\pi(\text{E0})$ and $\Omega_K(\text{E0})$ are electronic factors for the E0 pair creation decay and K-shell electron capture. We can then write the radiative decay width of the 4.98 MeV $0^+$ state as

$$\left(\frac{\Gamma_{rad}}{\Gamma}\right)^{4.98} = 1 = I_\gamma(\text{E2})\Bigg\{q_K^2(\text{E0/E2})\alpha_K(\text{E2})\left(1 + \frac{\Omega_\pi(\text{E0})}{\Omega_K(\text{E0})}\right) + 1 + \alpha_\pi(\text{E2}) + \alpha_K(\text{E2})\Bigg\}, \tag{2.16}$$

sorting this to solve for $I_\gamma(\mathrm{E2})$ gives us

$$I_\gamma(\mathrm{E2}) = \Big\{1 + \alpha_\pi(\mathrm{E2}) + \alpha_K(\mathrm{E2}) + q_k(\mathrm{E0/E2})\alpha_K(\mathrm{E2})\left(1 + \frac{\Omega_\pi(\mathrm{E0})}{\Omega_K(\mathrm{E0})}\right)\Big\}^{-1}. \quad (2.17)$$

The values of the terms presented in Equation 2.17 are as presented in Table 2.2[32]. Inserting for the values found in the table results in an intensity for the E2 gamma ray transition of

$$I_\gamma^{4.98}(\mathrm{E2}) = 0.9983, \quad (2.18)$$

which means that assuming that the majority of decay from the 4.98 MeV $0^+$ state in $^{28}$Si is from E2 gamma ray transitions is acceptable. Using the same method of solving for the intensity $I_\gamma(\mathrm{E2})$ in the radiative width to calculate the intensity for the 4.44 MeV $2^+$ in $^{12}$C results in

$$I_\gamma^{4.44}(\mathrm{E2}) = \frac{1}{1 + \alpha_\pi(\mathrm{E2}) + \alpha_K(\mathrm{E2})} = 0.9987. \quad (2.19)$$

This calculation also supports the assumption that majority of decay from the 4.44 MeV $2^+$ state in $^{12}$C is from E2 gamma ray transitions. Notice that there is a lack of E0-transition terms in Equation 2.19 because the only possible decay from this state is a $2^+ \rightarrow 0^+$-transition. Same procedure for the 1.78 MeV $2^+$ state in $^{28}$Si where the intensity of the E2 transitions can be written as

$$I_\gamma^{1.78}(\mathrm{E2}) = \frac{1}{1 + \alpha_\pi(\mathrm{E2}) + \alpha_K(\mathrm{E2})} = 0.9987. \quad (2.20)$$

Which again supports the assumption that the majority of decay through this state is by E2 gamma ray transitions.

The argument that the majority of decay from these states happen through gamma decay, the absolute photopeak efficiency can be defined as the ratio of the number of protons detected in coincidence with a gamma ray to the number of protons populating the excited state in the target. The terms $\epsilon_{4.44}$, $\epsilon_{3.21}$, $\epsilon_{3.20}$ and $\epsilon_{1.78}$ can therefore be written as

$$1 \times \epsilon_{4.44} = \frac{N_{20}^{4.44}}{N_{singles}^{4.44}}, \qquad 1 \times \epsilon_{1.78} = \frac{N_{20}^{1.78}}{N_{singles}^{1.78}} \quad \text{and} \quad 1 \times \epsilon_{3.20} = \frac{N_{02}^{4.98}}{N_{singles}^{4.98}} \approx 1 \times \epsilon_{3.21}. \quad (2.21)$$

These equations will be used to estimate the absolute photopeak efficiency in the data analysis in subsection 4.2.3 and the results are presented in chapter 5.

| Term | $^{28}$Si(3.20 MeV) | $^{28}$Si (1.78 MeV) | $^{12}$C(4.44 MeV) |
|---|---|---|---|
| $\Omega_\pi$ | $6.213 \times 10^{10}$ | | |
| $\Omega_K$ | $2.960 \times 10^{7}$ | | |
| $\alpha_\pi$(E2) | $8.70(13) \times 10^{-4}$ | $2.080 \times 10^{-4}$ | $1.322 \times 10^{-3}$ |
| $\alpha_K$(E2) | $3.14(5) \times 10^{-6}$ | $8.580 \times 10^{-6}$ | $1.584 \times 10^{-7}$ |

**Table 2.2:** Table showing the values of the terms presented in Equation 2.17, Equation 2.19 and Equation 2.20[32].

## 2.9 Previous measurements

The radiative width of the Hoyle state has been deduced through various measurements several times since the state was experimentally observed in 1953[16]. The gamma decay branching ratio have been measured a total of nine times[4, 5, 6, 7, 8, 9, 10, 11]. In Figure 2.3 an overview of the results from these measurements can be seen, as well as the current adopted value calculated from all measurements performed before Kibédi (2019)[11]. Seeger (1963)[33] can be considered as an outlier[3], and Kibédi (2019)[11] is the most recent result and has not yet been included in the adopted value.

The values presented in Figure 2.3 used several different methods for observation and measurement of the radiative branching ratio of the Hoyle state. The first experimental value measuring the gamma decay from the Hoyle state was performed by Alburger *et al.* (1961)[4], performed using proton-gamma-gamma coincidences by populating the Hoyle state through a $^{12}$Be($^{3}$He, p)$^{12}$C-reaction with a beam energy of 2.2 MeV and two 5 in$\times$5 in NaI-detectors.

The second measurement that observed proton-gamma-gamma triple coincidences was from Obst *et al.* (1976)[10]. This measurement was the first to publish a spectra where the 3.21 MeV gamma ray de-exciting from the Hoyle State was observed directly[34]. The Hoyle State was populated through the $^{12}$C(p, p') reaction with a proton beam energy of 10.48 MeV and the scattered protons were measured at 150°. The gamma rays were detected by four NaI scintillator crystals placed at angles perpendicular to the beam line. Even if Obst *et al.* were the first to publish the direct observation of the 3.21 MeV gamma ray in their spectra they did not include any scale on the axis in their spectra, merely labeling the axis with "counts". The amount of proton-gamma-gamma coincidences obtained by Obst *et al.* would have been very useful to compare with the present measurement.

The value from Kibédi *et al.* is measured at 68%[11] higher than the current

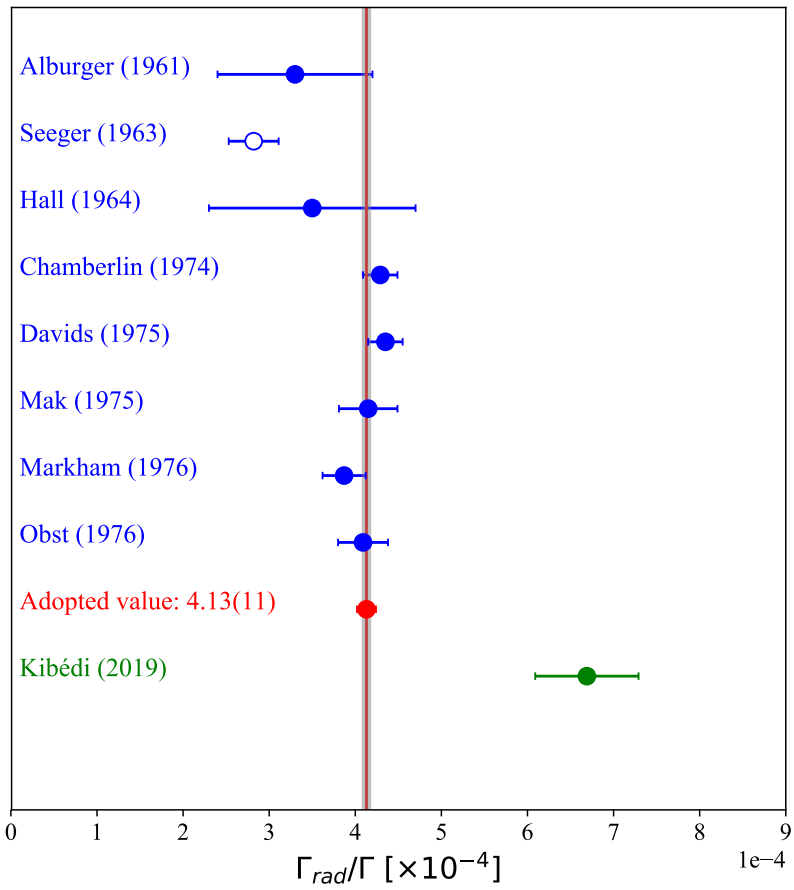


**Figure 2.3:** Figure showing all previous measurements of the ratio between the radiative width and the total width of the Hoyle state. Literature data from Alburger (1961)[4] , Seeger (1963)[33] which is omitted from the adopted value, Hall (1964)[5], Chamberlin (1974)[6], Davids (1975)[7], Mak (1975)[8], Markham (1976)[9] and Obst (1976)[10]. Kibédi (2019)[11] is also omitted from the adopted value due to the gap of time between Obst (1976)[10] and Kibédi (2019)[11]. Figure is originally from Kibédi (2019)[11] and has been modified with permission.

adopted value, marking a clear and sudden change in the series of measurements done on this ratio. The measurement was performed at the Oslo Cyclotron Laboratory in 2014 using the previous scintillation array stationed at the lab named CACTUS, which consisted of 28 NaI scintillation detectors, using SiRi[2] as the particle telescope. The measurement was performed using similar experimental set-up and analysis techniques as Obst *et al.*[10] used in 1976, as explained in section 2.6 and section 2.7.

It is still not understood clearly why the measurement from Kibédi *et al.* is so different from earlier measurements. However, it shows that there is a need to remeasure the radiative branching ratio to investigate the discrepancy between previous results, which is the goal of this thesis work.

# Chapter 3

# Experimental set-up and energy calibration

This chapter will give a description of how the experiment for the present work was done. Details about the detectors, the cyclotron as well as the calibration of the detectors will be explained thoroughly.

## 3.1 The Oslo Cyclotron Laboratory (OCL)

The experiment was performed at the Oslo Cyclotron laboratory, using the MC-35 Scanditronix cyclotron. This is one of the few cyclotrons available in Norway, located at the University of Oslo. It is used by several research fields and for different applications. The main fields of research are nuclear physics, nuclear chemistry and nuclear medicine. In Figure 3.1 is an outline of the OCL and its different research stations. A typical experiment in basic nuclear research consists of a light ion beam being accelerated in the MC-35 Scanditronix cyclotron before being guided out into the beamline. The available beams at the OCL are positively charged light ions such as protons, deuterons, $^{3}$He and $^{4}$He. After the beam has exited the cyclotron it will be guided through the beamline by several magnetic dipoles D and quadrupoles Q, used for bending and focusing the beam, respectively. At the end of the beamline a target chamber is located, with the particle telescope SiRi[2] and the scintillation array OSCAR.

### 3.1.1 OSCAR

Oslo Scintillator Array, or OSCAR[36], is a national infrastructure funded by The Research Council of Norway. OSCAR consists of 30 large volume $LaBr_3$(Ce) inorganic scintillator crystals, shown in Figure 3.2. It is stationed at the Oslo Cyclotron Laboratory and was officially opened in January 2019, during the experiment performed for this thesis. The cylindrical large volume detectors are 3.5 inches in diameter and

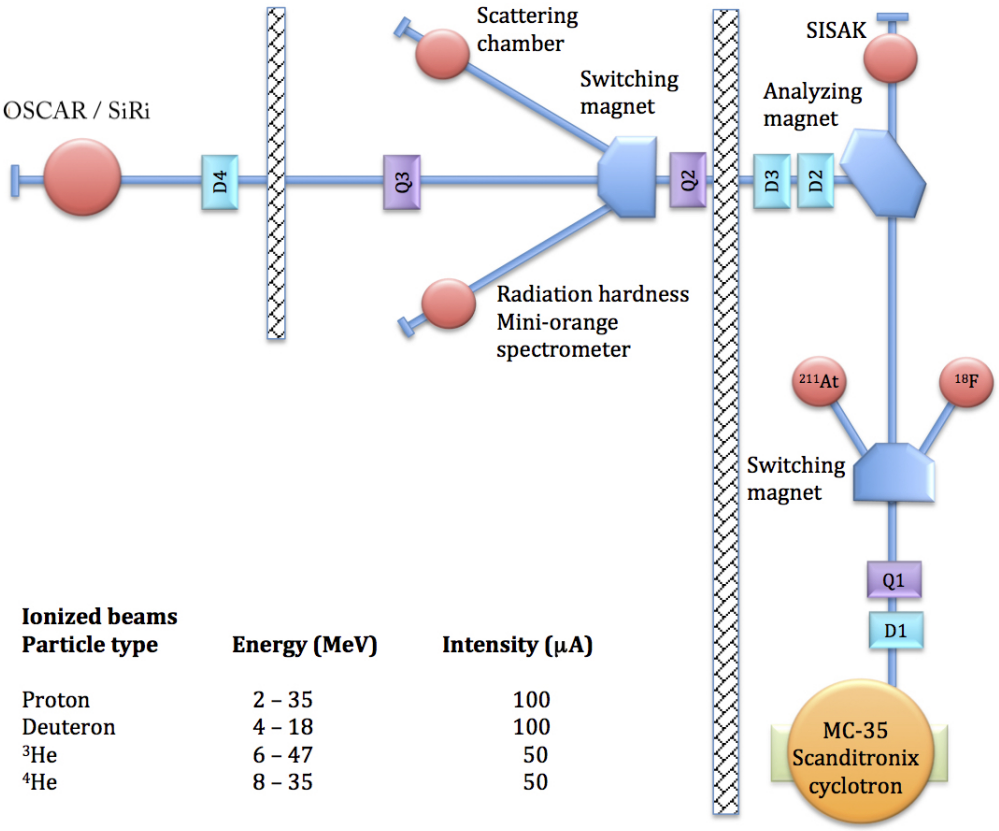


**Figure 3.1:** Outline of the OCL laboratory and its stations used for different research purposes, marked as red circles[35].

8 inches in height, making the absorption of high energy gamma rays ideal. OSCAR has an energy resolution of $\approx 2.7\% - 4.3\%$ at 662 keV gamma rays, and supreme timing properties with an intrinsic time resolution of $< 1$ ns[37]. The detectors are mounted on a icosahedron-shaped frame around the target chamber with a distance of 16.3 cm from the target, having a 57% of $4\pi$ angle coverage[31] at the time of the experiment performed for this thesis.

### 3.1.2 SiRi

SiRi(Silicon Ring)[2], shown in Figure 3.3a, is a semiconductor detector used for particle identification through the $\Delta$E-E telescope method. The detector system is designed for measurement of particle energy, time and discrimination between different charged light particles. Typically this is protons, deuterons, tritium or helium from transfer or scattering reactions. The telescope consists of eight two-layered trapezoidal shaped detectors. The thin front detector, $\Delta$E, is segmented into 8 curved pads covering mean scattering angles $\theta$ between 40° and 54° in increments of

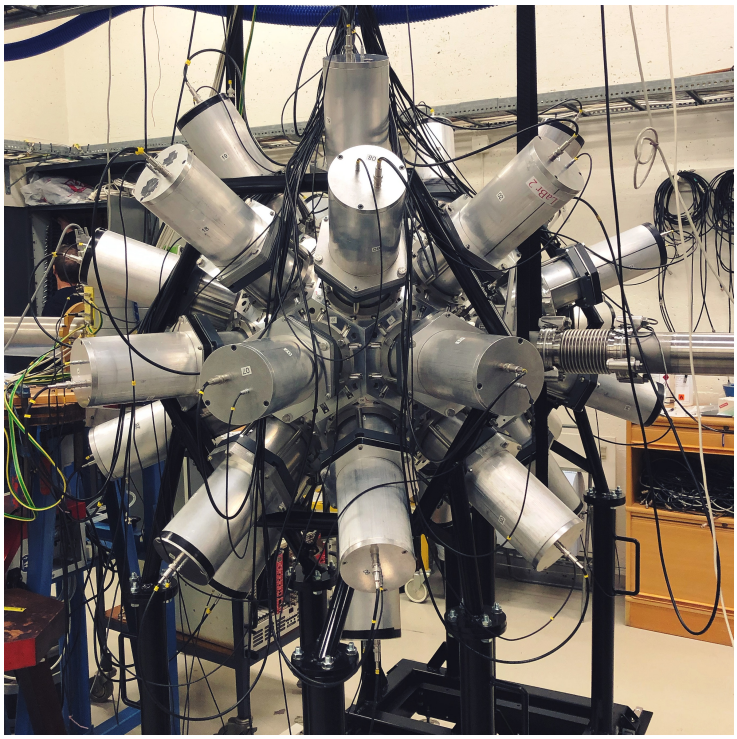

**Figure 3.2:** Picture of OSCAR fully closed around the target chamber.

2° per pad. If the detector is placed in backwards angle compared to the trajectory of the beam, the mean scattering angles $\theta$ will be between 126° and 140° in increments of 2° per pad. The thick E-detector is not segmented, but by requiring that only one $\Delta$E pad fires each event, pile-up events will be rejected[2]. Figure 3.3b shows the mounted telescope system within the target chamber. The front delta E detector has a thickness of 130 $\mu$m, while the E-detector has a thickness of 1550 $\mu$m.

### 3.1.3 Digital electronics and data acquisition

All events collected during the experiment performed during this thesis contain information about the energy and timing of signals from different detectors. When a particle hits the $\Delta$E-layer of SiRi charge carriers are collected, forming an electric pulse which passes through the digital pulse processors. Similarly when photons hit the active volume of $LaBr_3$-detectors of OSCAR, the gamma ray is converted into photons in the visible spectra and creating multiplied electrical signals which passes through the digial pulse processors. All detectors from SiRi and OSCAR are connected to the Multichannel Digital Gamma Finders (DGF) of type PIXIE-16, manufactured by XIA, the newly installed digital data acquisition system of OCL. Each detector of SiRi and OSCAR has its own channel, meaning that there are in total 64 channels for the $\Delta$E-layer and 8 channels for the E-layer of SiRi. Since OSCAR consists of 30 $LaBr_3$-detectors each detector has its own channel. Both layers

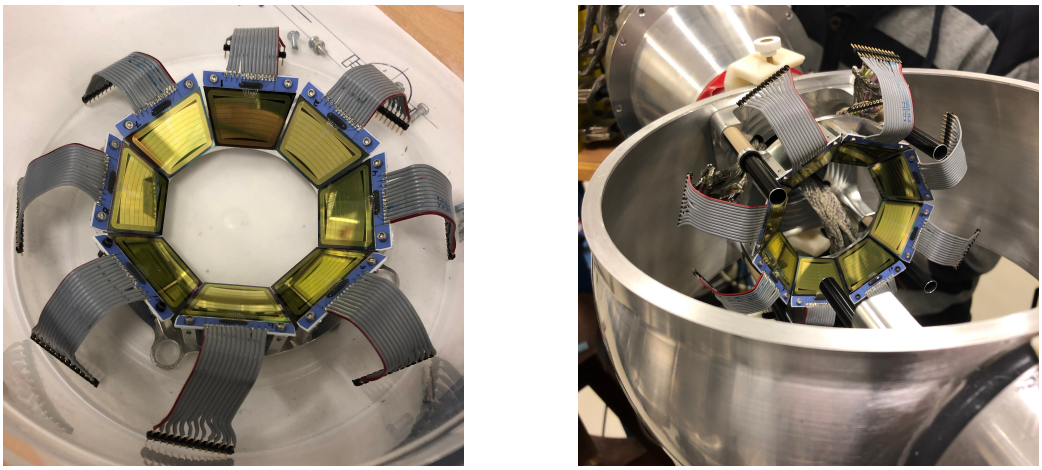

(a) (b)

**Figure 3.3:** The particle telescope SiRi seen from above in Figure 3.3a and mounted in the target chamber in backwards position in Figure 3.3b.

of SiRi were sampled with a frequency of 250 MHz, while the detectors of OSCAR are sampled with 500 MHz. The signals are stamped with energy and time values, passed through a net of optic cables, and stored in a computer disc in the control room of OCL.

All incoming data is processed by a validator that accepts or rejects events to prevent the mass storage of data that is not of interest during the experiment. During the experiment performed for this thesis the firing of the ΔE-layer of SiRi was chosen as the initiation of an event and all other detectors are digitally delayed to make them arrive after the detection of a particle in the ΔE-layer. In Figure 3.4 an illustration of the data acquisition is presented.

## 3.2 Proton-gamma-gamma experiment

The main experiment of this thesis work was done between the 28th of January 2019 and 8th of February 2019 at the Oslo Cyclotron Laboratory. The goal of the experiment is to measure the gamma decay branching ratio of the Hoyle state in $^{12}$C, using a $^{12}$C$(p, p'\gamma\gamma)$-reaction with a beam energy of 10.7 MeV. The protons emitted at angles between 140° and 126° relative to the beam line were detected by SiRi in coincidence with two gamma rays. The photons from the Hoyle state and the first excited state of $^{12}$C were detected by OSCAR. A figure illustrating the principle behind the experiment can be seen in Figure 3.5. Some beam time was also spent on a $SiO_2$ + $^{12}$C-target for the alternative calculation method of the gamma decay branching ratio, as explained in section 2.7. The reaction channel was $^{28}$Si$(p, p'\gamma\gamma)$, with the same detection principle as for $^{12}$C.

To populate the Hoyle state a beam energy of approximately 10.5 MeV is ideal, as one can deduct from the cross-section measured by C. Davids*et al.*[38] presented

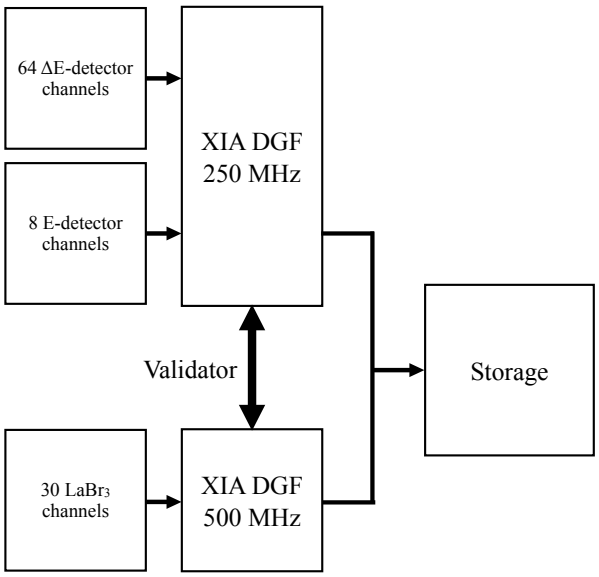


**Figure 3.4:** Illustration of the Data Aquisition System (DAQ) at OCL. Digital Gamma Finder (DGF) sample the detector signals from ΔE and E from SiRi(subsection 3.1.2) and OSCAR(subsection 3.1.1) and stamp them with a time and energy value in an event, and send them through optic fiber cables to be stored in a data storage disc.

in Figure 3.6. During the experiment performed by Kibédi *et al.* at OCL there was no significant difference in cross-section between a beam energy of 10.5 MeV and 10.7 MeV, therefore a beam energy of 10.7 MeV was chosen in 2014. Part of the reason this was tested was that a higher proton energy would shift the inelastically scattered protons well above the detecting threshold for the ΔE detector in SiRi[11].

J. Swint et al.[39] has investigated the differential cross-sections for populating states in $^{12}$C by inelastic scattering of protons at a series of angles and energies, as seen in Figure 3.7. The highest cross-section with a beam energy of 10.7 MeV is at the angle $\theta = 25.54°$, while the lowest cross-section is at the angle $\theta = 105.23°$. When SiRi is in backwards position the angle coverage was as earlier mentioned $126° - 140°$, while in forward position the angle coverage is $40° - 54°$. The low probability of detecting the desired proton-gamma-gamma-coincidences makes large amounts of statistics the highest priority, however, using SiRi in backwards position was chosen despite the low cross-section. This was to avoid large amounts of random coincidences and pile-up, where the largest component is the elastically scattered protons from the ground state of $^{12}$C, which mainly travels in forward direction. The $(p, \alpha)$-channel is an example of a highly populated channel which was less populated with the current set-up[10].

The considerably low beam energy of 10.7 MeV means that the protons emitted

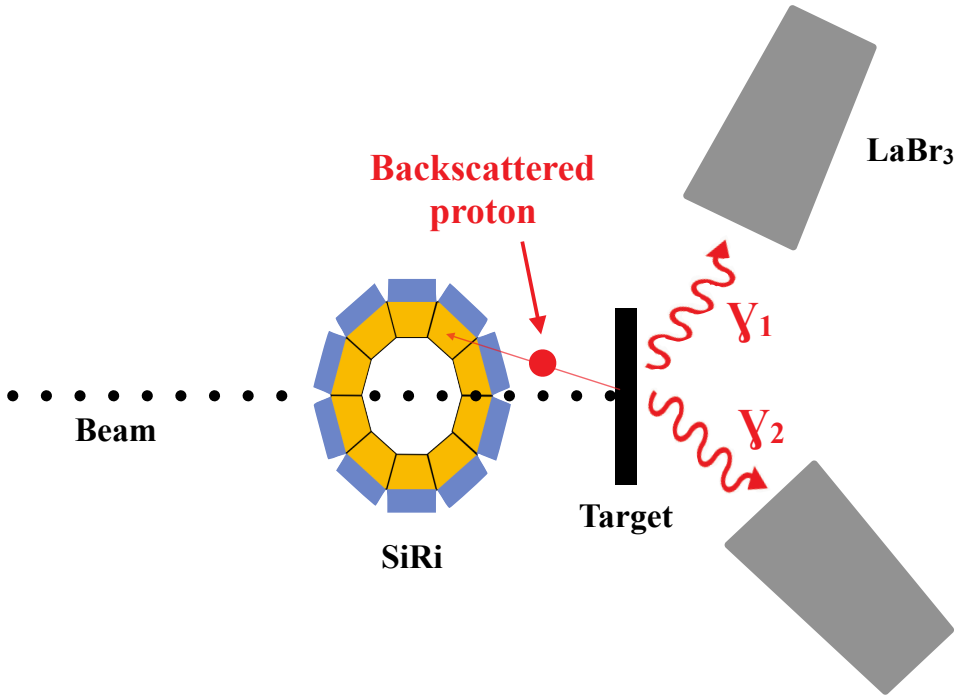


**Figure 3.5:** Illustration showing the initial beam hitting the target and the subsequent emittance of a proton and two gamma rays being detected by SiRi and OSCAR.

from the Hoyle state are not energetic enough to penetrate the first layer of the particle telescope, thus being stopped in the ΔE. This means that there is little possibility of removing background from the spectra. Thin targets were used to compensate for this problem, making the energy resolution of the particle spectra higher. However, the different channels could have been separated using the ΔE-E method of SiRi, so both forwards and backwards angles could have been used with a higher beam energy.

### 3.2.1 Target preparation

There were two main targets used during the experiment. The target used for direct measurements (see section 2.6) of the Hoyle state consisted of 180 $\mu$g of self-supporting Carbon-12 while the target used for a measurement using $^{28}$Si (see section 2.7) consisted of 140 $\mu$g of self-supporting $SiO_2$ with a thin layer of 30 $\mu$g $^{12}$C on the front side of the target.

The targets were provided by the Australian National University (ANU) and were mounted on aluminum frames from ANU. A total of 14 billion events were analysed from the data that was collected using the $^{12}$C target and 1.3 billion events were

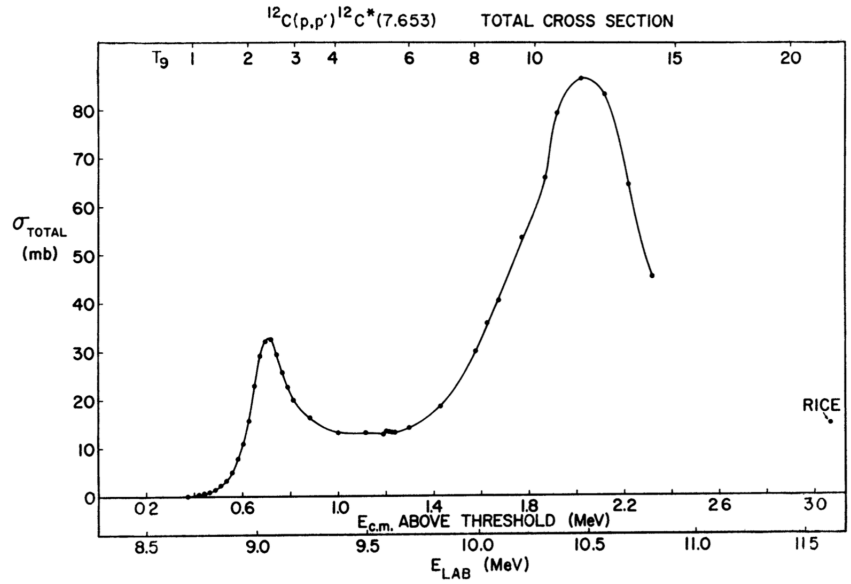


**Figure 3.6:** Figure from C. Davids et. al.[38] showing the total cross-section for populating the Hoyle state by inelastic proton scattering in the energy range $8.85 - 10.81$ MeV. The point marked "RICE" at around 11.6 MeV was obtained by J. Swint *et al.*[39].

analysed from the data using the $SiO_2$+$^{12}$C target.

## 3.3 Energy calibration

When a detector registers a signal, this signal is stored with a certain pulse height and time stamp. An experimental set-up can have many detectors, often signals from several detectors will be stored within nearly the same time-stamp. The characteristics of one detector is rarely the exact same as other detectors, even if both are of the same type. This is why calibration is necessary for all detectors included in an experimental set-up. This is done as a mathematical fitting between specific points of the raw data and information that is already known. This can be experimental data from a reliable nuclear database or through kinematic calculations of expected particle energies.

### 3.3.1 Particle telescope SiRi

We assumed a linear connection between the raw signals and the true energy of the signals for the particle telescope, SiRi[2]. Therefore the data was calibrated using a linear equation such that

$$\mathrm{E} = \mathbf{gain} \times \mathbf{channel} + \mathbf{shift}, \tag{3.1}$$

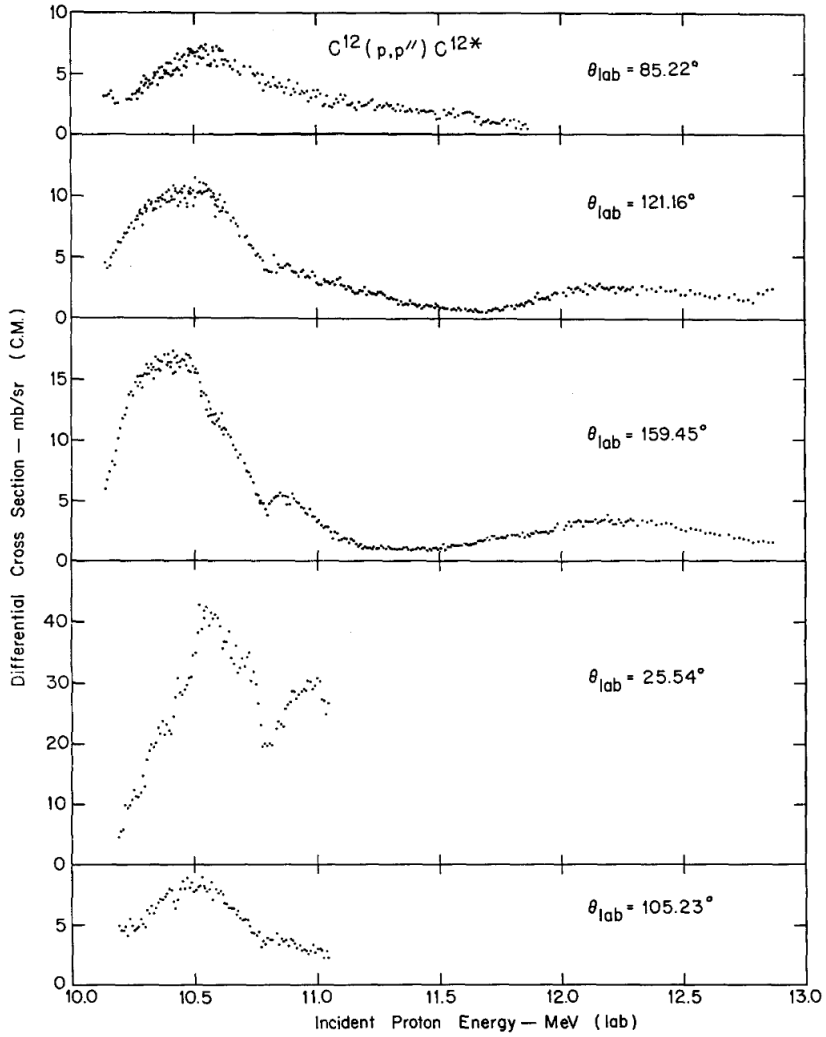


**Figure 3.7:** Figure from J. Swint *et al.*[39] showing the differential cross-sections for populating states in $^{12}$C by inelastic scattering of protons for several energies as well as emitted angle of the proton ejectile.

where channel is the raw signal in a specific channel and $E$ is the channel converted into energy, usually denoted in units of keV or MeV. To find the calibration parameters **shift** and **gain** a linear mathematical fitting must be done in this case. Specific characteristic points in the data were chosen as the calibration points, in this case the wise choice would be to choose the protons emitted from the excited states in the isotope they have inelastically collided with. The energy of the emitted proton, based on the incoming proton energy, can be predetermined using kinematic calculations, together with the energy these emitted protons will deposit in the different layers of the particle telescope. The particles energy loss in the medium it interacts with can

be described by the Bethe-Bloch formula[40] given as

$$-\frac{dE}{dx} = 2\pi N_{\mathrm{a}} r_{\mathrm{e}}^2 m_{\mathrm{e}} c^2 \rho \frac{Z}{A}\frac{z^2}{\beta^2}\left[\ln\left(\frac{2m_{\mathrm{e}}\gamma^2 v^2 W_{\max}}{I^2}\right) - 2\beta^2 - \delta - 2\frac{C}{Z}\right], \tag{3.2}$$

where each of the terms are described as follows:

- $r_{\mathrm{e}}$ : classical electron radius $= 2.817 \times 10^{-13}$cm
- $\gamma$ : $v/c$ of the incident particle $\gamma = 1/\sqrt{1-\beta^2}$
- $m_e$ : Electron mass
- $\delta$ : Density correction
- $N_a =$ Avogadro's number $= 6.022 \times 10^{23}$
- $C$ : Shell correction term
- $I$ : Mean excitation potential
- $W_{max}$ : Maximum energy transfer in one collision
- $Z$ : Atomic number of absorbing material
- $A$ : Atomic weight of absorbing material
- $\rho$ : Density of absorbing material
- $z$ : Charge of incident particle in units of $e$

As seen in Equation 3.2 one can differentiate the energy loss in a medium of same density based on the charge and the mass of the particle traveling through the matter. This principle is what the SiRi detector utilizes by having a detector that is segmented into two layers. In the current work the only particle channel that was of interest was the $(p, p')$-reaction, however it can also be used to identify several different channels, differentiating between the outgoing particles. A typical plot using both layers of the particle telescope can be seen in Figure 3.8, showing the calibrated data from the $SiO_2$ + $^{12}$C-target where the signals from the ΔE-E detector can be seen along the y- and x-axis, respectively. The particle signals that are mainly visible here are from protons and deuterons, as no other channels are strongly populated in this reaction. Several peaks can be seen in the 'banana-shaped' plot for the protons, these correspond to states in the different ions present in the target material. The area consisting of signals from the $(p, p')$-reaction include protons populating the nuclei $^{12}$C, $^{16}$O and $^{28}$Si. To identify excited states from these nuclei in the spectra one can begin with the fact that energy and momentum is conserved, this means that we can use kinetics calculations to calculate what the incoming and outgoing particle

energies will be. The different peaks can be identified roughly by the fact that the protons populating the nuclei with the largest mass will lose the least energy in the collision with the nucleus, resulting in the proton detected having an energy close to the initial energy. The protons populating the ground state in $^{28}$Si will therefore leave the least energy in ΔE and the most in E. We can therefore roughly sort the peaks by the mass of the nuclei involved in the reaction. The corresponding particle energies for these states for both ΔE and E can be calculated using Qkinz[41], a kinematics calculation program designed for OCL. Using these facts means that it is possible to identify all states visible in the particle spectra. However, for the excited states the most secure method is to also gate on the detected proton peaks and compare with the signals from the OSCAR-array to identify the gamma rays from the different excited states in the nuclei.

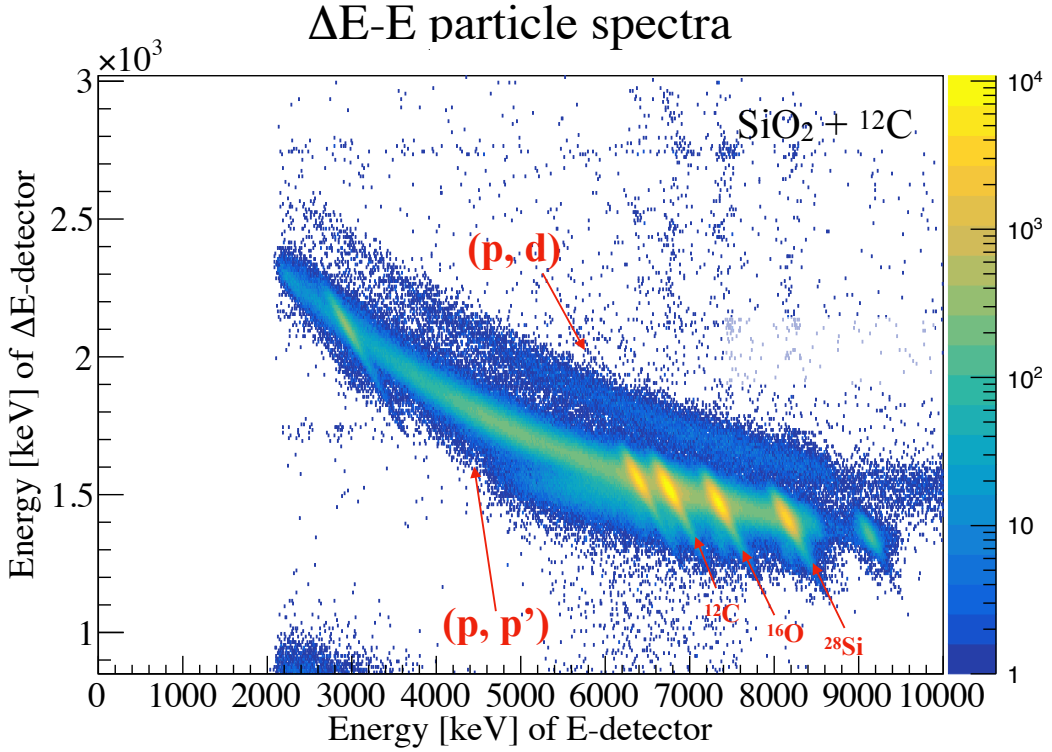


**Figure 3.8:** ΔE-E plot of the particle telescope SiRi for the $SiO_2$ + $^{12}$C target. Different reaction channels and the ground state of three isotopes are marked by red arrows.

Two separate calibrations were done for the particle telescope because there are two different isotopes of interest. Firstly the ΔE-detectors were calibrated using the different states of interest in both $^{12}$C and $^{28}$Si. In Figure 3.9 a histogram shows the particle spectra for events that had E-detector multiplicity **mult** = 0 or **mult** = 1. The events containing **mult** = 0 are protons which are stopped in the ΔE-layer of the detector, while **mult** = 1 means that the proton penetrated the ΔE-layer

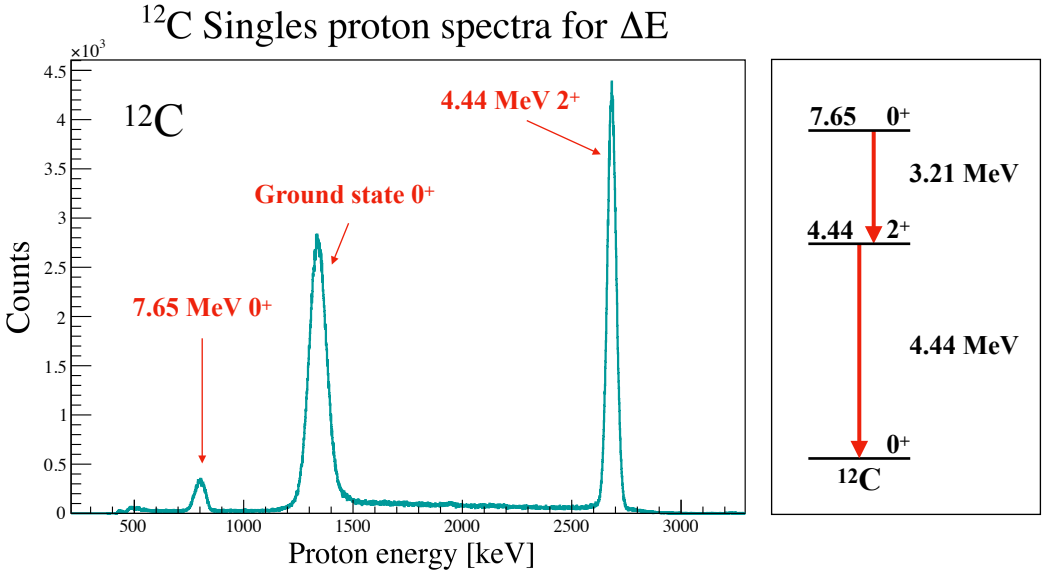


**Figure 3.9:** Left panel: Histogram showing a portion of the data collected in the ΔE-detector strips from the $^{12}$C-target. The different states have been marked with red arrows. Right panel: The level scheme for the first few levels of $^{12}$C and their gamma decay transitions, red arrows highlight the gamma decay transitions of interest.

and also deposited energy in the E-layer. The right panel of Figure 3.9 shows the different excited states populated by the protons, and the corresponding level scheme and gamma-decay transitions from these excited levels. The two levels of interest are the 7.65 MeV Hoyle state and the first excited state 4.44 MeV in $^{12}$C, therefore these two points were used for calibrating the ΔE-layer of SiRi. In Figure 3.10 the particle spectra with both multiplicities for the $SiO_2$+$^{12}$C-target as well as the corresponding gamma decay scheme for the populated levels of $^{28}$Si are shown. As seen in the text boxes in the left panel there are several nuclei whose excited levels have been populated by the protons. In the right panel red arrows mark the gamma ray transitions of interest in the data analysis, as explained in section 2.7. The levels these gamma ray transitions originate from are the 1.78 MeV $2^+$ and the 4.98 MeV $0^+$ states. These were chosen as the calibration points for the ΔE-layer of SiRi, along with the 6.69 MeV $0^+$ state as a middle point between the two states. The 1.78 MeV $2^+$ was chosen as an approximate value because the peak including this state is quite broad in the spectra presented in Figure 3.10.

### 3.3.2 Problems with the particle telescope SiRi

During the experiment, the threshold of the E-detector of SiRi[2] was set to an unusually high value, causing all protons with an energy lower than $2 \sim 3$ MeV to be discarded in the E-detector. However, the associated signal in the ΔE-layer is still

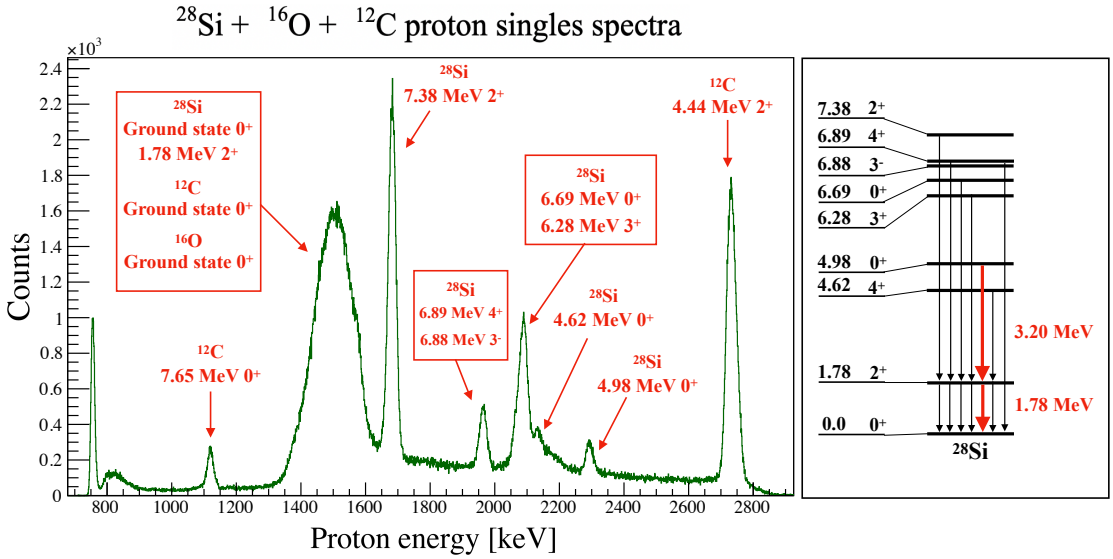


**Figure 3.10:** Left panel: Histogram showing a portion of the data collected in the ΔE-detector strips from the $SiO_2$+$^{12}$C-target. The different states have been marked and identified with red arrows and text boxes. Right panel: The level scheme for the identified levels of $^{28}$Si and their gamma decay transitions, red arrows highlight the gamma decay transitions of interest.

recorded. This means that we cannot subtract background from the particle spectra, and there was no data from the E-detectors used in the analysis. The consequences of this is not fully understood, but as long as peaks are well separated in the spectra an analysis is possible. Because of this threshold there are states which should have been recorded in the E-detector which are only visible in the ΔE-detector. One example of this is the first excited state of $^{12}$C at 4.44 MeV. Kinematic calculations of the recoiling proton energy using Qkinz[41] show that this state will penetrate the ΔE-layer of the detector and be stopped in the second E-layer. However, as shown in Figure 3.11 this state is not visible in the ΔE-E spectrum. The same problem of missing states can be seen in the data for $^{28}$Si, where a $0^+$ state at 4.98 MeV should have been visible in the E-detector as shown in Figure 3.12 as well as the 4.62 MeV $0^+$ state which has only partly penetrated the ΔE-layer.

There is also a ground state visible at approximately 9.2 MeV in the E-detector from an unknown element. No specific element has been discovered as a contaminant in the target or elsewhere in the data, but it is clear that it is much heavier than $^{28}$Si from the fact that the protons detected from inelastically colliding with this nucleus lost very little energy, meaning that the nucleus had very little recoil. This causes the detected protons total energy to be close to the beam energy of 10.7 MeV. An investigation into the possible mass ranges using Qkinz[41] yielded around $^{72}$Ge to $^{127}$I as possible elements, not considering the probability of the specific element being present in the data. As this element is not visible elsewhere in the data, the cause and

origin of this peak was not investigated further in this thesis. In all files pad number 8 is missing because of a faulty connection, the data from the associated ΔE-pad is still intact but had to be discarded.

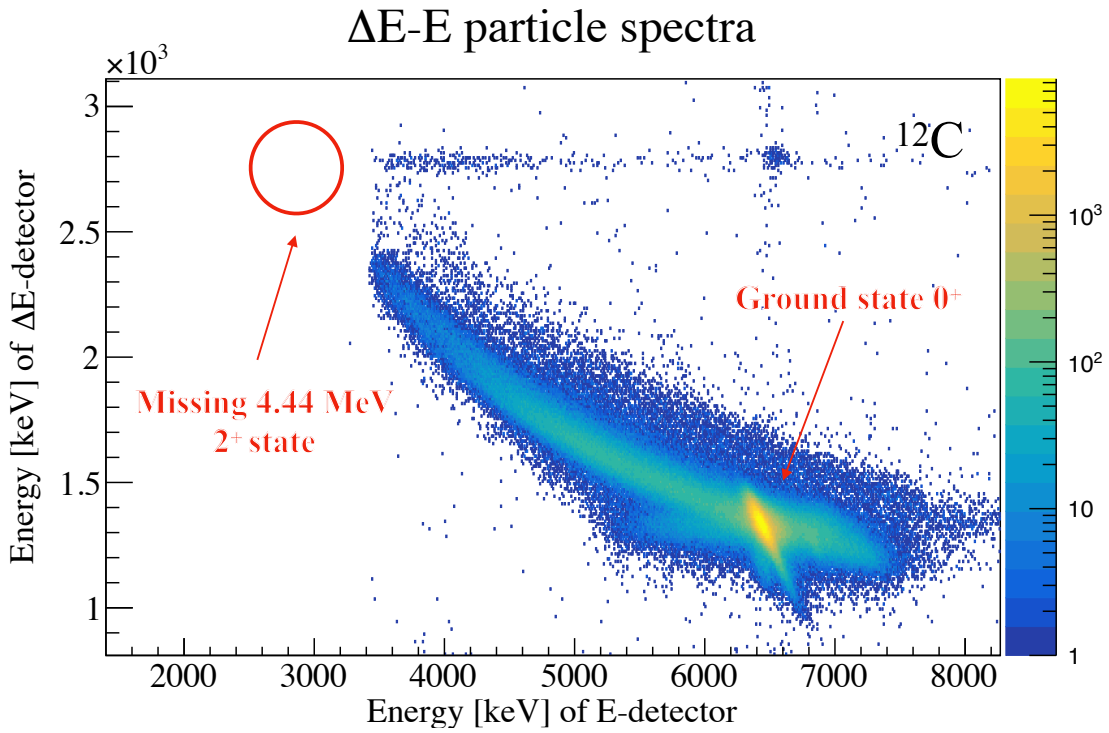


**Figure 3.11:** Matrix showing the ΔE-E spectra for the $^{12}$C-target where the different excited states has been pointed out with red arrows. The missing 4.44 MeV $2^+$ state is also pointed out.

### 3.3.3 Photon detector array OSCAR

For the $LaBr_3$ array OSCAR a polynomial of second order was used for calibrating the signals in the detectors. The formula used to calibrate the raw signal into energy $E$ is

$$E = \mathbf{gain}_2 \times \mathbf{channel}^2 + \mathbf{gain}_1 \times \mathbf{channel} + \mathbf{shift}, \tag{3.3}$$

where $\mathbf{gain}_1$, $\mathbf{gain}_2$ and **shift** are parameters chosen through the mathematical fit. Since the fit is a second order polynomial it is important to choose calibration points in the region of interest, as the accuracy of the calibration will decrease outside of the chosen region of the mathematical fit. For the current data, the region of interest is a gamma ray energy between 1.78 MeV and 4.44 MeV. These transitions are presented in Figure 3.9 and Figure 3.10.

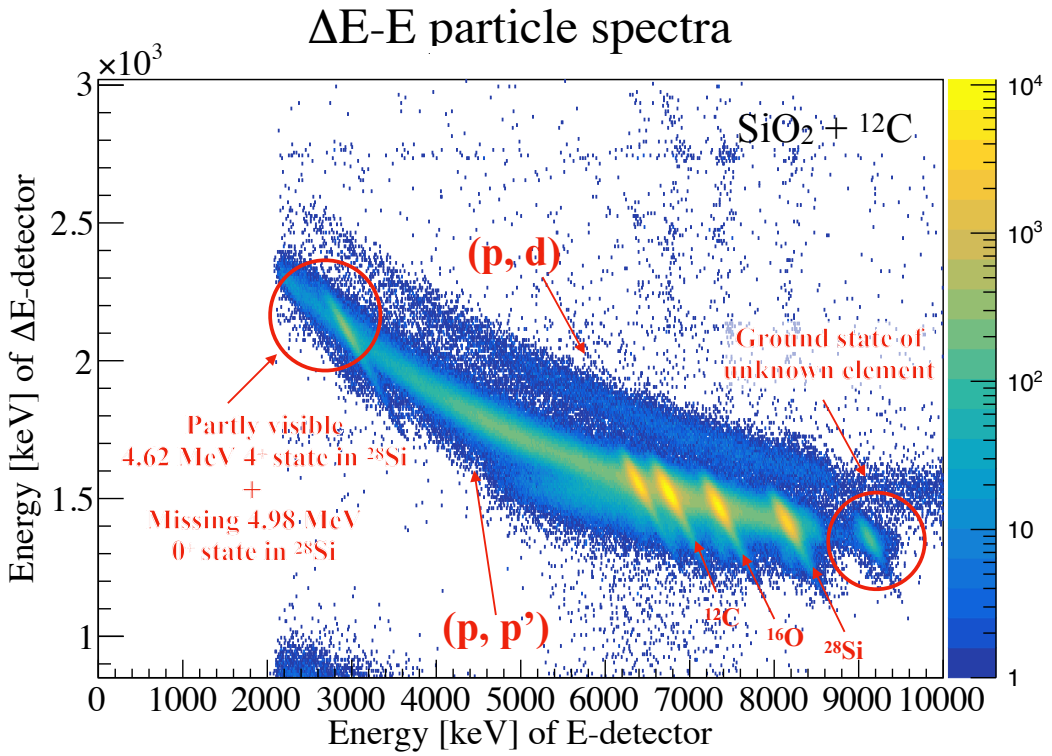


**Figure 3.12:** Matrix showing the ΔE-E spectra for the $SiO_2$ + $^{12}$C-target where the different excited states in $^{28}$Si has been pointed out with red arrows. The 4.62 MeV $4^+$ state and the 4.98 MeV $0^+$ state are missing.

In Figure 3.13 a calibrated histogram showing the energy of all $LaBr_3$-detectors for a set of data using the $^{12}$C-target can be seen, together with two panels showing the level schemes for the visible gamma ray transitions. A variety of these peaks were used as calibration points, chosen over the whole energy range. It is clearly visible in this spectra that $^{27}$Al is a strong background component from protons hitting the frame of the target, however, this contaminant also gave calibration points over a wide range of energies. Another component which can contribute to background or peaks in the photon spectra is the internal radiation of the $LaBr_3$-detectors themselves[42].

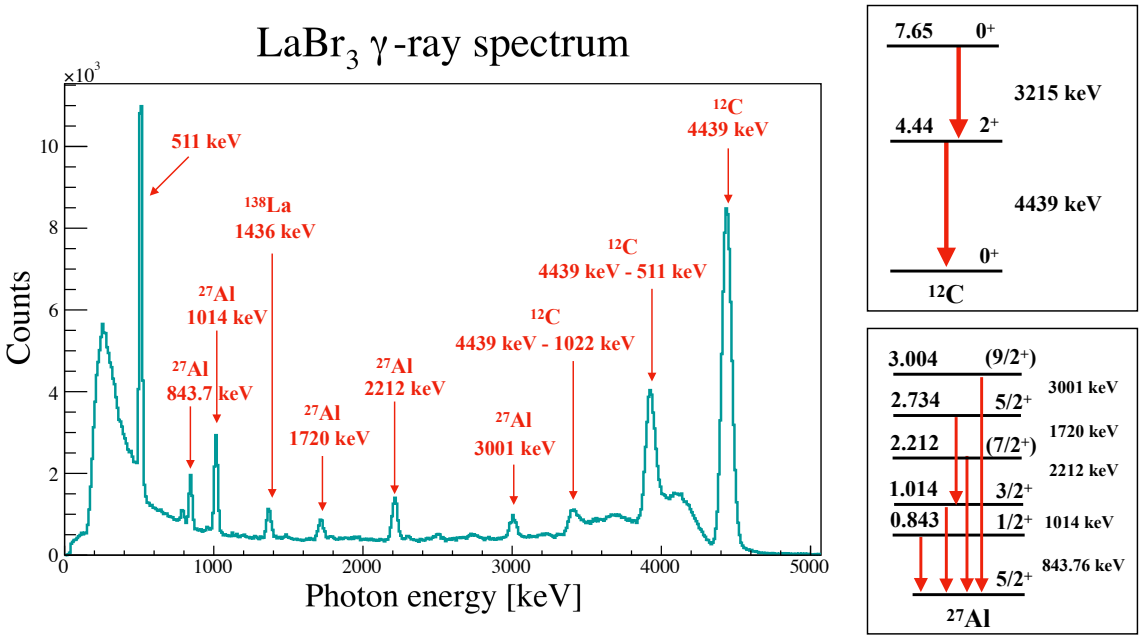


**Figure 3.13:** Left panel: Histogram showing the energy of all $LaBr_3$-detectors for a set of data using the $^{12}$C-target, arrows point to the different identified states. One peak from $^{138}$La originating from the internal radiation[42] of the $LaBr_3$-detectors of OSCAR is present at 1436 keV. Right panel: Level schemes and the relevant states and transitions visible in the spectra is shown in the two boxes as well as arrows pointing to the respective gamma ray transitions. $^{27}$Al originates from protons hitting the frame of the target and is a contaminant in the spectra, however it was also used for calibration.

# Chapter 4

# Data analysis

This chapter explains the process behind the analysis of the data collected in the experiment performed in this thesis. The most important concepts in the analysis will be explained in detail, such as how the proton-gamma-gamma coincidences are sorted and how a background subtraction is performed on the photon spectra. The analysis behind each term in the radiative width of the Hoyle state as given in Equation 2.12 is explained thoroughly.

The data analysis is based on the sorting of the information behind what is called an event. An event contains all the information recorded by the data acquisition system during a time interval $\Delta$t and is defined by the corresponding time stamp provided by the trigger. One can sort the information from a single event using different methods, for example gating on time or energy. One can define what triggers an event by the triggering of a signal in a detector. What was selected to detect the gamma cascade from the Hoyle state is a triple coincidence consisting of a proton-gamma-gamma coincidence, naturally the triggering of an event in this experimental set-up was the detection of a particle in SiRi[2].

## 4.1 Photon spectra

OSCAR is needed to observe the gamma-cascade emitted from the Hoyle State in coincidence with the proton. The events that we are interested in are events where there is a single signal from each of the gamma rays emitted from the Hoyle state. To investigate the average multiplicity of $LaBr_3$ behind an event, a sorting of the multiplicity was done on a portion of the data. This is presented in Figure 4.1 which shows the multiplicity of $LaBr_3$-detectors per event. From Figure 4.1 it is clear that a substantial amount of the events are recorded with a multiplicity equal to one. These events are not relevant to this analysis and will therefore not be used. What is relevant is the events with multiplicity larger than one, however, events with multiplicity larger than two will have an increasing possibility of random coincidences with increasing multiplicity. To make sure all events of interest are recorded, a series of requirements

for each signal was performed before acceptance: For the data collected using the $^{12}$C-target an event should have *one* signal in the energy range of the 3.21 MeV gamma ray, *one* signal in the energy range of the 4.44 MeV gamma ray and the angle between these two detectors is checked so that the event is sorted in the appropriate spectra. The angle between the two detectors is important because of the angular correlation coefficienct, as explained in section 2.6.

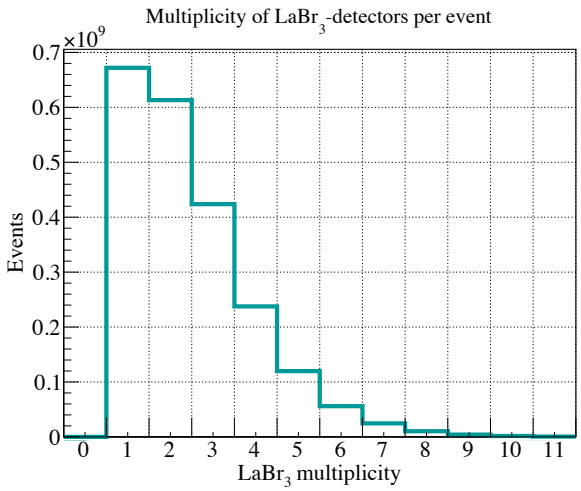


**Figure 4.1:** Histogram showing the multiplicity of $LaBr_3$-detectors per event.

Another method used in the analysis of this data was to present the detector signals in a matrix. We can build a matrix showing the photon energy in each of the detectors along the axes. By sorting the signals of the first detector along the x-axis and the other detectors along the y-axis we make sure not to record the signal from the same detector twice in the same matrix. Even if there is some degree of asymmetry in the plot, this will not have any impact as all events from all detectors are recorded there only once.

This matrix $M$ can be defined as a function which can have several types of constraints such that

$$M(t, E, m), \tag{4.1}$$

where $t$ denotes a time constraint, $E$ an energy constraint and $m$ a $LaBr_3$ multiplicity constraint. As for the multiplicity constraint it will be $m > 1$ for all measurements of the proton-gamma-gamma coincidences using OSCAR.

### 4.1.1 Subtraction of random coincidences

A substantial percentage of the events recorded by OSCAR are from materials other than the target material which is activated during the experiment, these signals are

grouped into components called background or contamination. Background can be categorized into two components: Constant background and background in coincidence with true events. Examples of constant background is the internal radiation from the $LaBr_3$-detectors of OSCAR consisting of signals from $^{138}La$ and $^{227}Ac$[42]. Examples of background which is in coincidence with true events is gamma ray signals from $^{27}Al$, originating from the frame that the targets are mounted upon. The cross-section of $^{27}Al$ is very high and the target frame is thick, resulting in high levels of background from aluminum even if only a tiny fraction of the beam hits the frame. This type of background comes with the beam pulse, as the peak structure along the axes in Figure 4.2 show. Contamination is a term used for unwanted presence of isotopes in the target which results in peak structures from this nuclei in the data. Background events, random or in coincidence, as well as signals from contamination nuclei are signals that are unwanted in the data and should be removed if possible.

Background which is not in coincidence with true events can be removed. By using the method of sorting the signals from the $LaBr_3$-detectors into a matrix, we can investigate the timing between the detectors of OSCAR. A matrix containing the timing between two $LaBr_3$-detectors can be seen in Figure 4.2.

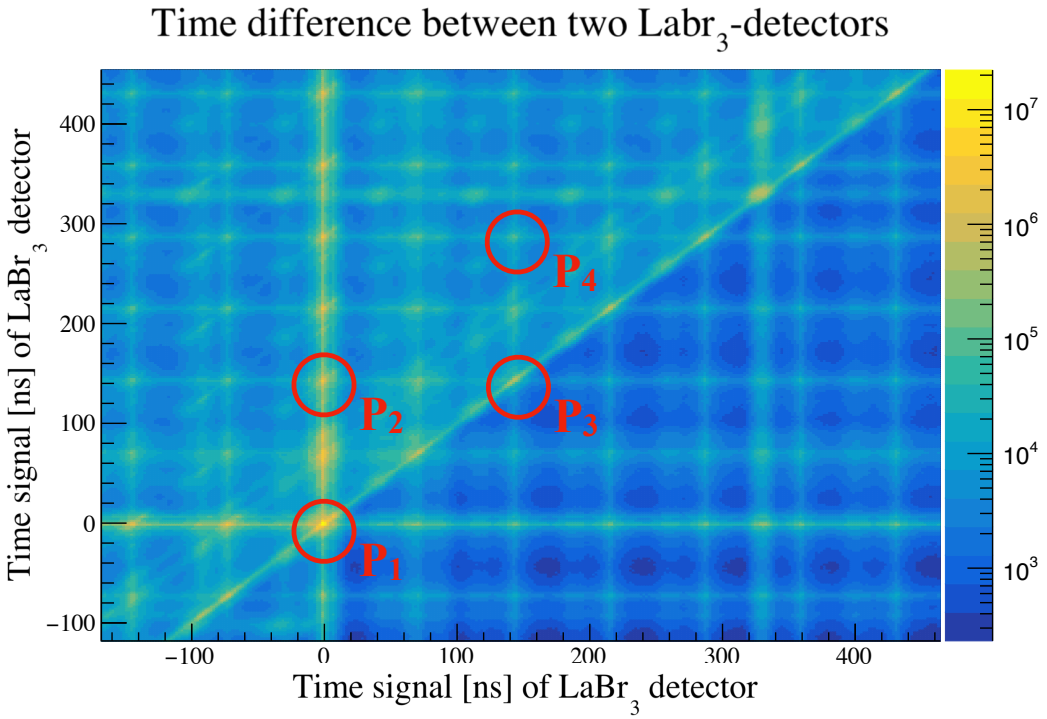


**Figure 4.2:** Matrix showing the timing between events giving signals in two $LaBr_3$-detectors.

In Figure 4.2 there are several characteristics marked in red circles. The signal at around zero for both detectors are the true coincidence with the proton for the events, in other words the prompt-prompt-prompt coincidences, this is marked as

| Peak | Signal $p - \gamma_1 - \gamma_2$ |
|---|---|
| $P_1$ | prompt-prompt-prompt coincidence |
| $P_2$ | prompt-prompt-delayed coincidence |
| $P_3$ | prompt-delayed-delayed coincidence |
| $P_4$ | delayed-delayed-delayed random |

**Table 4.1:** Table showing the points which are marked in Figure 4.2 and the characteristics of these points corresponding to their appearence in time.

$P_1$. The area marked as $P_2$ are the signals from the other detector or detectors from different beam bursts compared to the first one, this peak is thus a prompt-prompt-delayed coincidence. The point $P_3$ lies along the diagonal and is therefore a proton in coincidence with two gammas from a different beam burst, since all $LaBr_3$-detectors are delayed in time. The peak $P_3$ is therefore a prompt-delayed-delayed coincidence. The last peak $P_4$ is, following the earlier arguments, is defined as a delayed-delayed-delayed coincidence where both protons and gammas are from different beam bursts. An overview of the different points and their corresponding signal appearance in time can be seen in Table 4.1.

These characteristic points can be used to remove random coincidences from the total spectrum of the $LaBr_3$-detectors. This is because the marked areas can be defined as nearly constant background, as is also visible in the matrix in Figure 4.2 in further delayed peaks. By using the defined points $P_1$, $P_2$, $P_3$ and $P_4$ as time constrictions when filling matrices with events we can remove the undesired random coincidences. We can now define an equation which produces a matrix where all random coincidences are removed:

$$M_{\text{clean}} = M(t = P_1) - M(t = P_2) - M(t = P_3) + M(t = P_4). \tag{4.2}$$

The reason that $M(P_4)$ is added and not subtracted from $M_{\text{clean}}$ is that the same background is subtracted through the points $M(t = P_2)$ and $M(t = P_3)$. This is to avoid subtracting too much information from the matrix, as we are measuring a quantity with very low statistics.

### 4.1.2 Photon spectra

A coincidence matrix for a large portion of the data taken with a $^{12}$C-target can be seen in Figure 4.3 and in Figure 4.4 for the $SiO_2$ + 12C-target. This matrix has

no energy constraints and random coincidences have been subtracted according to Equation 4.2. Even with a background-subtraction large amounts of signals from the aluminum frame are visible in both gamma-gamma matrices. These coincidences are marked with $^{27}$Al as we assume that most of the frame consists of the isotope $^{27}$Al. A possible consequence of this is a surplus of aluminum events in the peaks of interest for the analysis, resulting in a larger peak area or increased amount of background in the spectra. To calculate the number of proton-gamma-gamma coincidences the signals presented in the gamma-gamma matrices in Figure 4.3 and Figure 4.4 are needed, making signals from aluminum a possible disturbing component in the data analysis. To reduce this source of uncertainty a gate was required on the area of interest in the gamma-gamma matrix, which was used to fill spectra with protons in coincidence with these gamma rays. The result is a proton spectra where the aluminum coincidences are either non-existent or dispersed in the background. This means that disturbance or possible contribution to the background in the analysis from aluminum will be minimal, even if the ideal situation is that aluminum was not present in spectra.

There are also large amounts of coincidences between two 4.44 MeV gamma rays in Figure 4.3. These coincidences cannot originate from the proton-gamma-gamma coincidences, as there is only a single 4.44 MeV gamma ray in the gamma cascade from the Hoyle state. These 4.44 MeV coincidences originate from the $LaBr_3$-detectors detecting photons from events where protons populating the 4.44 MeV $2^+$ state are not detected by SiRi. These events containing two 4.44 MeV gamma rays in coincidence will not affect the amount of proton-gamma-gamma coincidences from the Hoyle state, since the gating on the gamma-gamma matrix will be used to sort a spectra containing only the protons, as explained earlier in this section. The protons in coincidence with the two 4.44 MeV gamma rays will not be registered at the energy of the proton originating from the Hoyle state.

## 4.2 The gamma decay branching ratio

The following sections describe the data analysis methods used to calculate the different terms in the gamma decay branching ratio of the Hoyle state. As a reminder, in section 2.6 the ratio is given as

$$\left(\frac{\Gamma_\gamma^{\mathrm{E2}}}{\Gamma}\right)^{7.65} = \left(\sum_{\theta=0}^{180} \frac{N_{020}^{7.65}(\theta)}{C_\theta \times W_{020}^{7.65}(\theta)}\right) \frac{1}{K} \times \frac{1}{N_{\mathrm{singles}}^{7.65} \times \epsilon_{3.21}/M \times \epsilon_{4.44}/M} \tag{4.3}$$

As described in section 2.7, removing the dependency of the angular correlation coefficient using $^{28}$Si the branching ratio becomes

$$\left(\frac{\Gamma_\gamma}{\Gamma}\right)^{7.65} = \frac{N_{020}^{7.65}}{N_{020}^{4.98}} \times \frac{N_{\mathrm{singles}}^{4.98}}{N_{\mathrm{singles}}^{7.65}} \times \frac{\epsilon_{1.78}}{\epsilon_{4.44}} \times \frac{\epsilon_{3.20}}{\epsilon_{3.21}} \times \frac{W_{020}^{4.98}}{W_{020}^{7.65}}. \tag{4.4}$$

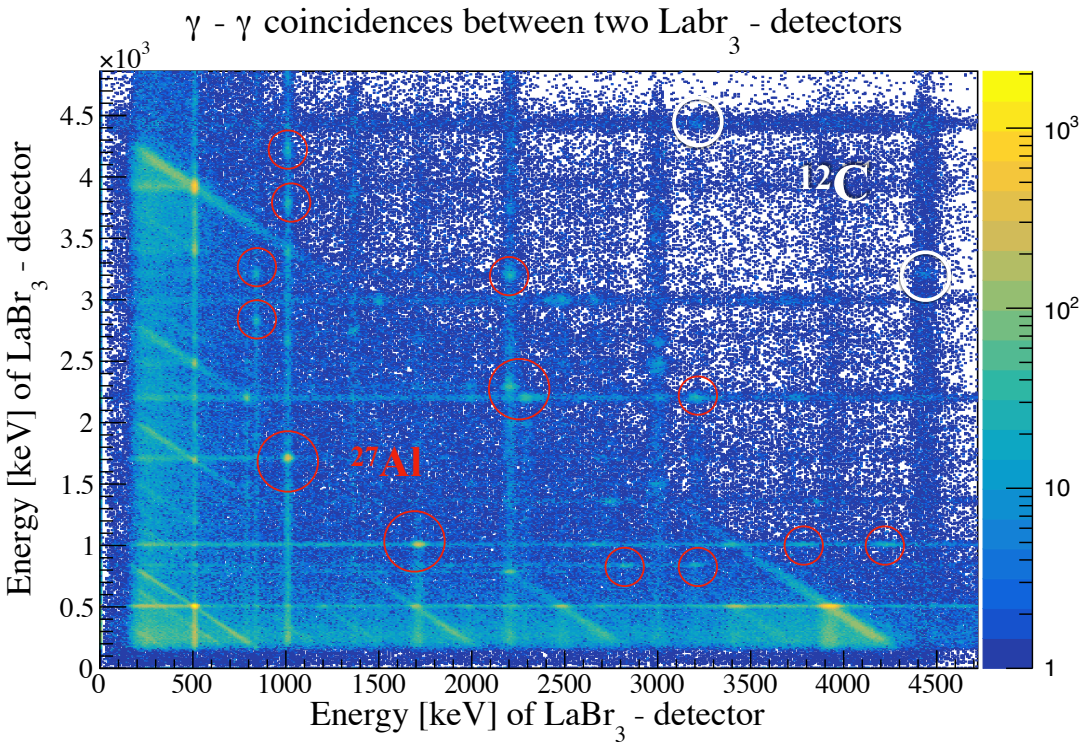


**Figure 4.3:** Coincidence matrix of the data collected on the $^{12}$C-target. The data is sorted by gating on protons populating the Hoyle state, random coincidences are subtracted according to Equation 4.2. The gamma-gamma coincidences from the Hoyle state are shown in white circles. Background coincidences from proton-gamma-gamma coincidences $^{27}$Al is shown in red circles. Unmarked peaks originate from coincidences from different cascades or nuclei.

### 4.2.1 Proton singles yield

The term describing the total number of protons which populated the excited states we are determining the gamma decay branching ratio from are the terms

$$N_{\text{singles}}^{7.65} \quad \text{and} \quad N_{\text{singles}}^{4.98}. \tag{4.5}$$

These are defined as the total number of protons populating the Hoyle state at 7.65 MeV in $^{12}$C and the 4.98 MeV state in $^{28}$Si. The terms are therefore the sum of all protons that are emitted in coincidence with the gamma cascades we want to detect as well as all protons emitted in coincidence with other decay paths, such as the $\alpha$-breakup. Calculating these terms from the data is uncomplicated and straightforward. By sorting the calibrated data such that a histogram containing all events that populated only the $\Delta$E layer in the SiRi-detector we get a histogram such as shown in Figure 4.5, which shows data from the $^{12}$C-target. Also shown in this histogram is an enlarged section around the Hoyle state at 7.65 MeV. The red shaded area is the

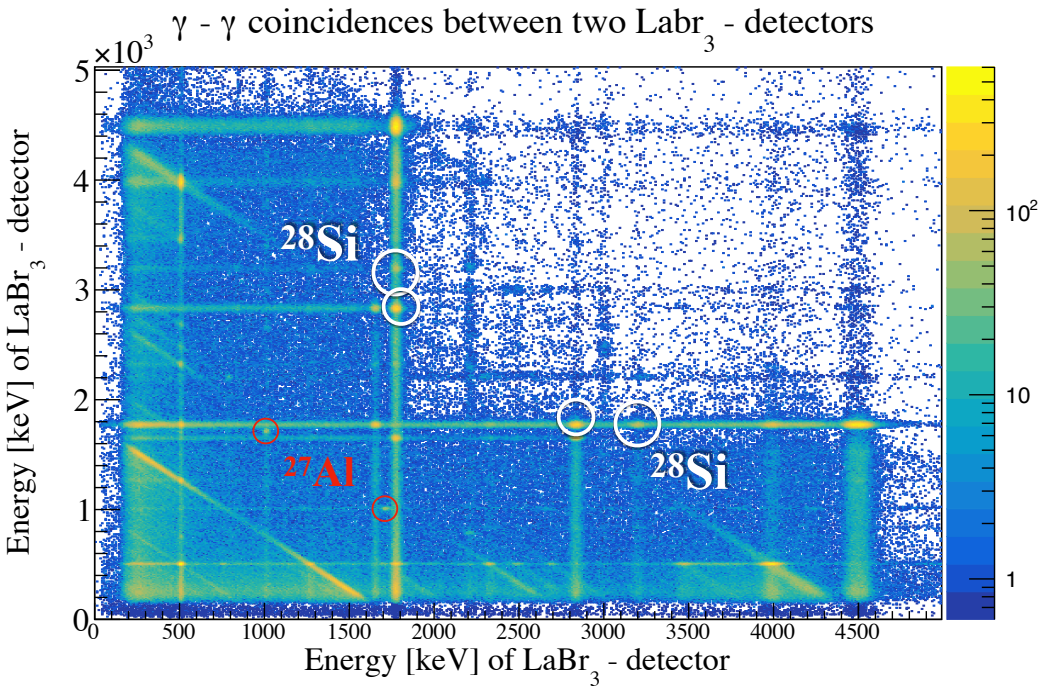


**Figure 4.4:** Coincidence matrix of the data collected on the $SiO_2$+$^{12}$C-target. The data is sorted by gating on protons populating the 4.98 Mev $0^+$ state in $^{28}$Si, random coincidences are subtracted according to Equation 4.2. The gamma-gamma coincidences from $^{28}$Si are shown in white circles. Background coincidences from proton-gamma-gamma coincidences $^{27}$Al is shown in red circles. Unmarked peaks originate from coincidences from different cascades or nuclei.

fit used to calculate the term $N^{7.65}_{\text{singles}} = 3.44 \times 10^8$.

The same procedure is used to calculate the proton singles in the term $N^{4.98}_{\text{singles}} = 7.6 \times 10^6$ from the $^{28}$Si-target. The red shaded area of Figure 4.6 shows the fit that was used to calculate the proton singles of the 4.98 MeV $0^+$ state in $^{28}$Si.

### 4.2.2 Proton-gamma-gamma coincidence yield

The proton-gamma-gamma coincidence yield is the term describing the amount of emitted protons which resulted in a specific gamma cascade from the excited nucleus. In the case of $^{12}$C this is protons populating the 7.65 MeV Hoyle state in coincidence with a 3.21 MeV gamma, followed by the 4.44 MeV gamma from the first excited state. For $^{28}$Si this term describes the protons populating the 4.98 MeV excited state in coincidence with a 3.21 MeV gamma and the following 1.78 MeV gamma from the first excited state. The term describing the proton-gamma-gamma coincidence yield

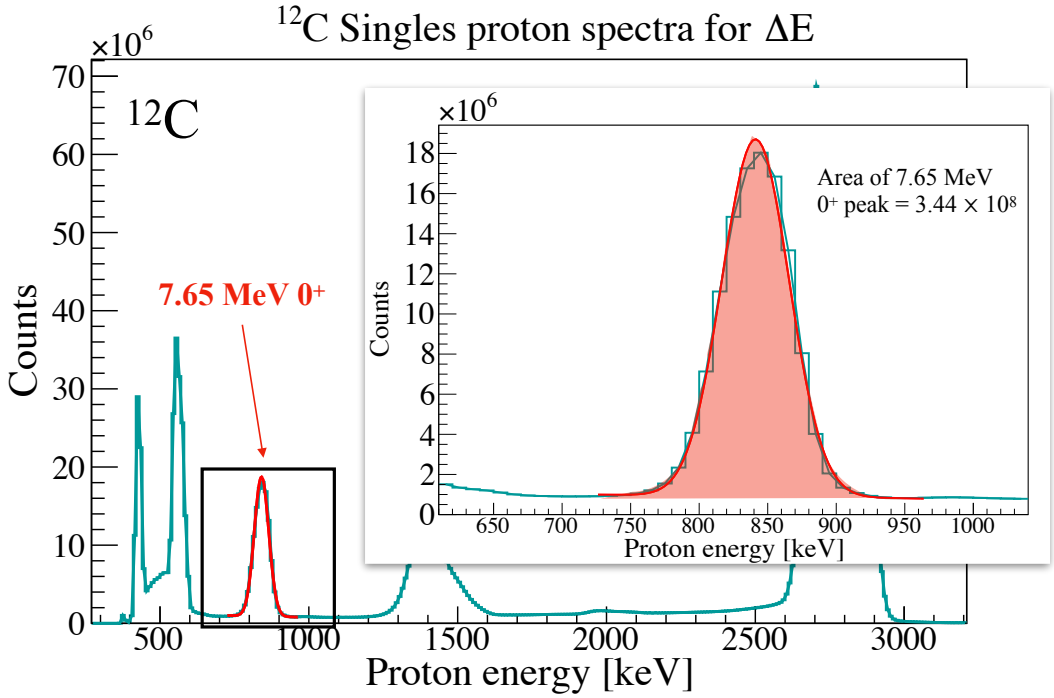


**Figure 4.5:** Singles particle spectra from the ΔE-detector from $^{12}$C data. The area around the Hoyle state is marked and magnified to show which peak is included in the calculation of the number of proton singles.

in Equation 4.3 is

$$\left(\sum_{\theta=0}^{180} \frac{N_{020}^{7.65}(\theta)}{C_\theta \times W_{020}^{7.65}(\theta)}\right) \frac{1}{K}. \tag{4.6}$$

The terms describing the proton-gamma-gamma coincidence yield of $^{12}$C and $^{28}$Si in Equation 4.4 are

$$N_{020}^{4.98} \quad \text{and} \quad N_{020}^{7.65}.$$

Since these three terms describe a proton in coincidence with two gamma rays, the method of calculating these terms is through gating on these gamma rays both in energy and in time. In Figure 4.7 a gamma-gamma matrix containing data from the $^{12}$C target is shown. The red circles mark the area in the matrix where there is coincidence between a 3.21 MeV gamma and a 4.44 MeV gamma, which is the gamma cascade from the Hoyle state that we want to measure. By requiring a single gamma ray in the 3.21 MeV energy region and a single gamma ray in the 4.44 MeV region when sorting the events we will create a histogram containing the protons which came in coincidence with the measured gamma rays in the gated area.

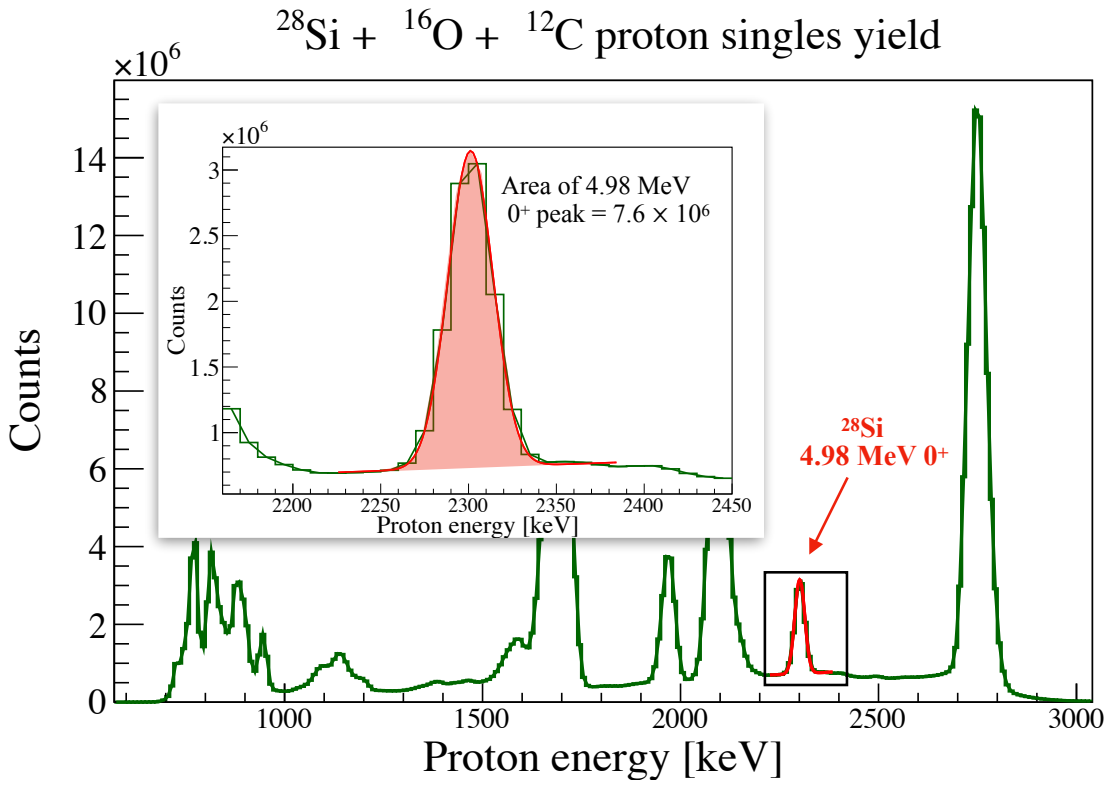


**Figure 4.6:** Singles particle spectra from the ΔE-detector from $^{28}$Si+$^{12}$C data. The area around the 4.98MeV $0^+$ state is marked and magnified to show which peak is included in the calculation of the number of proton singles.

This gating was done in the sorting of the gamma-gamma matrix and the background subtraction of the $LaBr_3$-detectors. This means that the term $N_{020}^{7.65}$ is also background subtracted according to the same method as the $LaBr_3$-detectors. The resulting histogram showing the protons that were emitted in coincidence with the detected gamma rays using Equation 4.4 can be seen in Figure 4.8. The proton-gamma-gamma coincidences sorted to be used in Equation 4.3 can be seen in Figure 4.9. By comparing Figure 4.9 and Figure 4.8 a significant difference of two magnitudes can be seen in number of counts in the 4.44 MeV and 7.65 MeV peaks. This difference originates from the correction according to both the angular correlation $W_{020}^{7.65}(\theta)$ between the two gamma rays, but also according to the number of detector combinations $C_\theta$ for each angle and the total number of angles $K$ used in the sum. These variables will adjust the proton-gamma-gamma coincidences $N_{020}^{7.65}(\theta)$ to be the average number of proton-gamma-gamma coincidences in a given detector angle combination between two detectors of OSCAR. As expected there will be no counts for protons corresponding to the ground state of $^{12}$C in neither Figure 4.8 or Figure 4.9. The 4.44 MeV peak is significantly reduced compared to the 4.44 MeV peak in the singles proton yield spectra showed in Figure 4.5. However, this state is

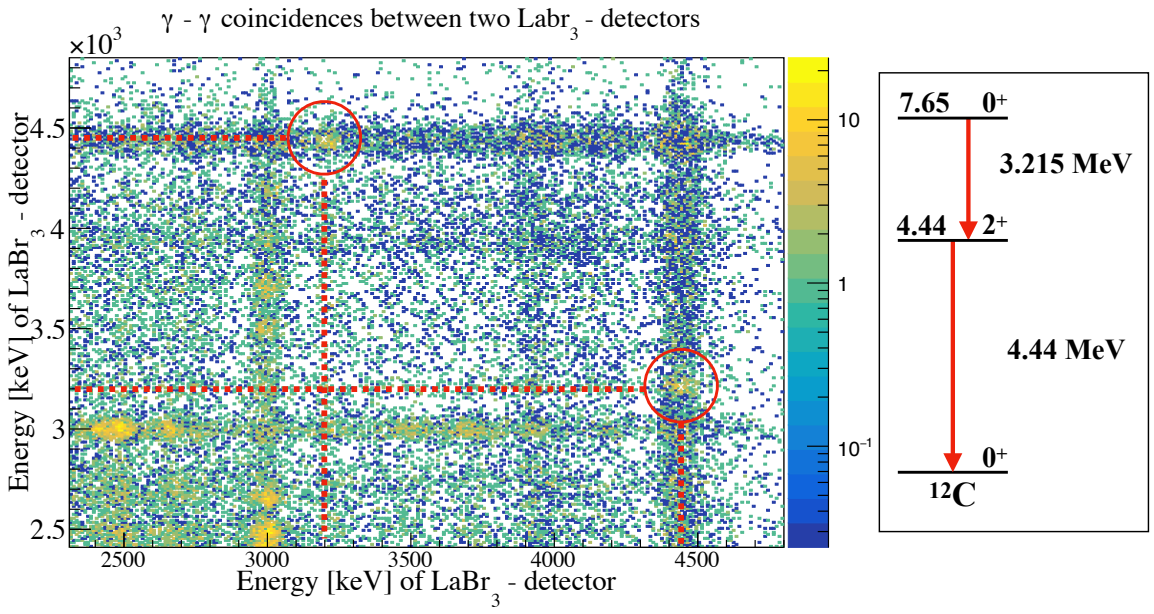


**Figure 4.7:** Left panel: A section of the coincidence matrix shown in Figure 4.3. The red circles show the coincidences between the 3.21 MeV and 4.44 MeV photons originating from the Hoyle state. Right panel: Level scheme showing the excited levels and the gamma ray transitions visible in the gamma-gamma matrix for $^{12}$C.

strongly populated as described in subsection 4.1.2, which is the reason why there are still a large amount of counts even after gating on the coincidence area. The 7.65 Hoyle state peak is reduced to nearly nothing, this is as expected when the currently measured probability of decaying to the ground state is $\approx 0.06\%$[28].

The gamma-gamma matrix for $^{28}$Si is shown in Figure 4.10. Red circles mark the area where the 3.20 MeV gamma ray and the 1.78 MeV gamma ray are in coincidence. This will also be the area gated on when sorting for protons which are in coincidence with these gamma rays. The proton-gamma-gamma coincidence yield is shown in Figure 4.11. The proton-gamma-gamma coincidence yield histogram has several proton peaks in coincidence with the two gamma rays from the 4.98 MeV state, with the most populated peak being the 4.98 MeV state itself. These other peaks originate from other states in $^{28}$Si which are heavily populated and emits two gamma rays in coincidence with the emitted proton. There is also a wide unknown peak in the area around the 4.98 MeV state, the origin of this peak is so far not known. Because the peak is quite broad there are reasons to believe this might be from the frame which the target is mounted upon, thus originating from an excited state in $^{27}$Al. The SiRi-detector in itself is also made of silicon, which also makes it a possible source of this broad peak.

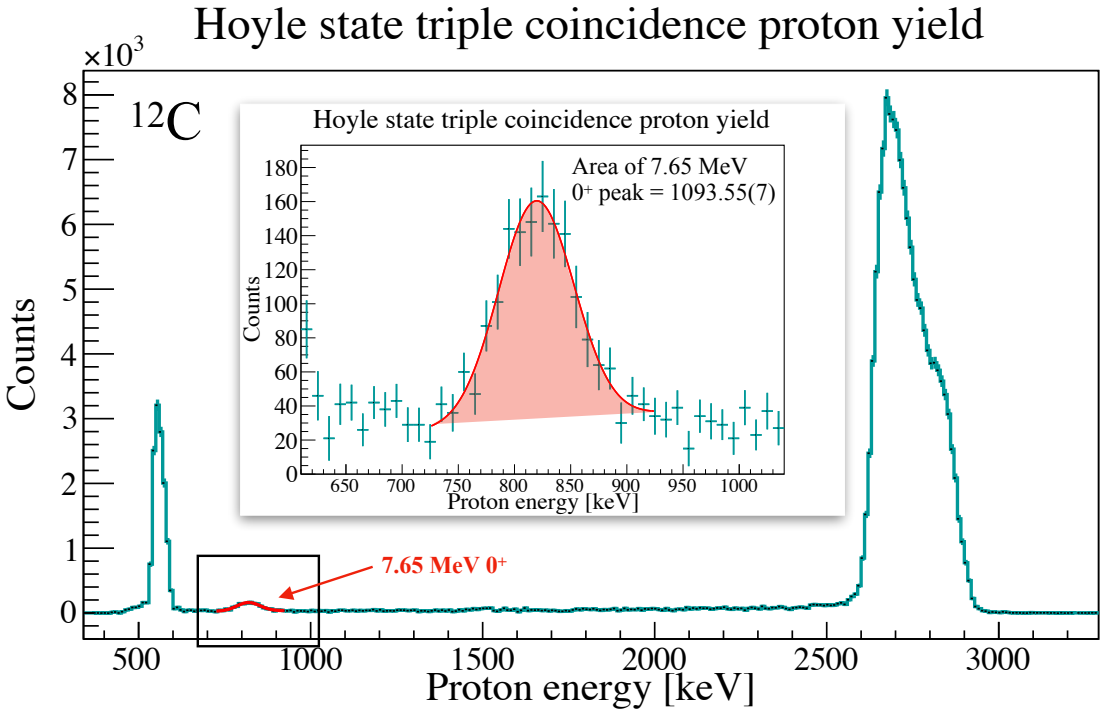


**Figure 4.8:** Triple-coincidence yield proton spectra from $^{12}$C data requiring a single gamma ray in the 3.21 MeV energy region and a single gamma ray in the 4.44 MeV energy region. The area around the Hoyle state is marked and magnified to show which peak is included in the calculation of the proton-gamma-gamma coincidence yield, the red shaded area shows the area of interest. The area obtained in this sorting will be used as the term $N_{020}^{7.65}$ in Equation 4.4.

### 4.2.3 Absolute photopeak efficiency

The absolute photopeak efficiency is needed at the following energies:

$$\epsilon_{1.78}, \quad \epsilon_{3.20}, \quad \epsilon_{3.21} \quad \text{and} \quad \epsilon_{4.44},$$

where $\epsilon_{3.21}$, $\epsilon_{4.44}$ are from $^{12}$C and $\epsilon_{3.20}$, $\epsilon_{1.78}$ are from $^{28}$Si. As mentioned in section 2.8 the absolute photopeak efficiency is normally calculated using Equation 2.13 and a radioactive source of known activity. There was no such measurement done during the experiment performed for this thesis, so two other methods were used to estimate the efficiency. The first method, as explained in section 2.8, used protons populating states decaying mostly by gamma decay to estimate the ratio of detected and emitted gamma rays, by using the ratio between gamma rays detected and protons populating the state. This method was used on two sets of data and the resulting efficiencies were compared to each other. The first set of data was the data for the $SiO_2$-target collected for this thesis, and the second set of data was a calibration run populating $^{28}$Si through the $(p, p')$-reaction using a beam energy of 16 MeV, collected in November

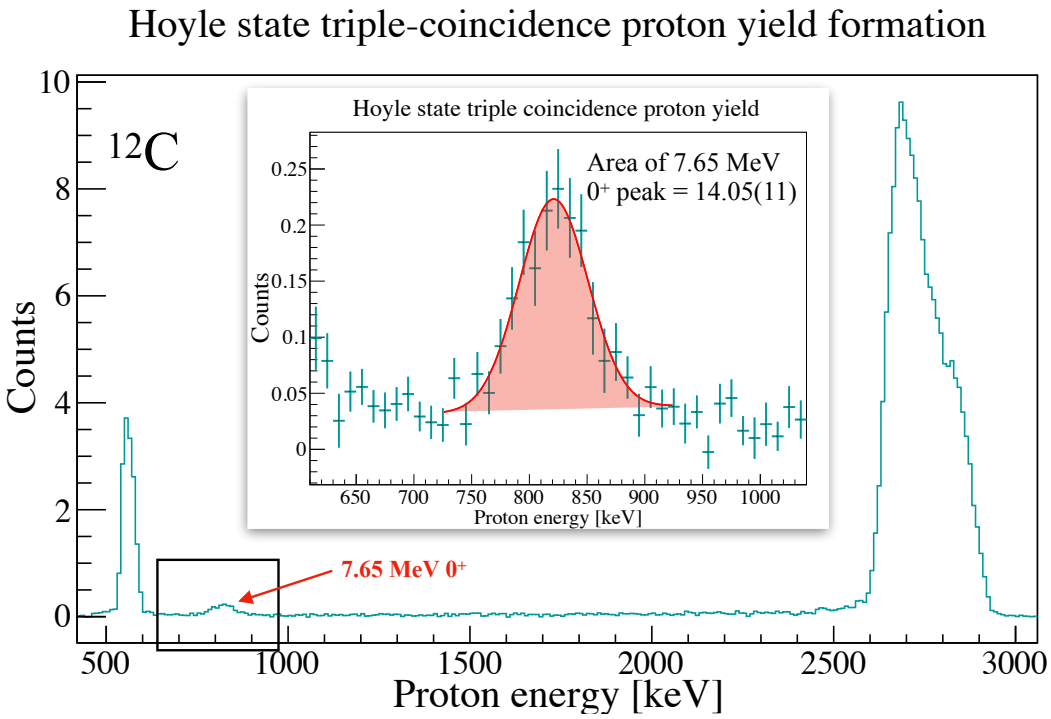


**Figure 4.9:** Triple-coincidence yield proton spectra from $^{12}$C data requiring a single gamma ray in the 3.21 MeV energy region and a single gamma ray in the 4.44 MeV energy region. The data is also adjusted for the angular distribution as described in subsection 4.2.4. The area around the Hoyle state is marked and magnified to show which peak is included in the calculation of the proton-gamma-gamma coincidence yield, with the red shaded area showing the fit of the peak. The area from this sorting will be used in Equation 4.3.

and December of 2019. A second set of data was used to compare the efficiencies because the data collected for this thesis had several states in $^{28}$Si missing in the E-detector, as described in subsection 3.3.2. A beam energy of 16 MeV on a $^{28}$Si means that all states used for the estimation of the efficiency are visible in the E-detector, making it much easier to properly gate on states and remove background in the spectra. The second method used a function for the absolute photopeak efficiency of OSCAR made by F. Bello[43], constructed by measuring several different radioactive sources at several energies.

The resulting measured efficiency for $\epsilon_{1.78}$, $\epsilon_{3.20}$, $\epsilon_{3.21}$ and $\epsilon_{4.44}$ are presented in Table 4.2. The measurements of the absolute photopeak efficiency in Table 4.2 performed during this thesis have been included in the measured absolute photopeak efficiency graph made by F. Bello[43] in Figure 4.12. The fit to the data does not include the efficiencies from $^{28}$Si and $^{12}$C, these are added afterwards.

In the direct method of calculating the gamma decay branching ratio of the Hoyle state(see section 2.6) the absolute photopeak efficiency of OSCAR at $\epsilon_{3.21}$ and $\epsilon_{4.44}$ are

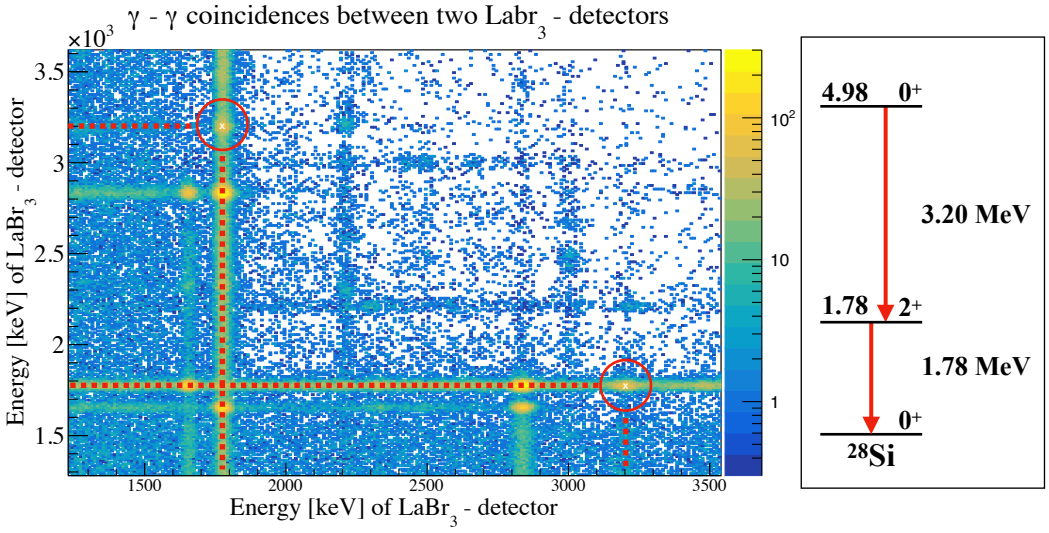


**Figure 4.10:** Left panel: A portion of the coincidence matrix shown in Figure 4.4. The red circles show the coincidences between the 3.20 MeV and 1.78 MeV photons originating from the 4.98 MeV $0^+$ state in $^{28}$Si. Right panel: Level scheme showing the excited levels and the gamma ray transitions visible in the gamma-gamma matrix for $^{28}$Si.

used directly, as seen in Equation 4.3. For the method using the 4.98 MeV $0^+$ state in $^{28}$Si as a method of canceling the angular correlation coefficient(see section 2.7) two of the efficiency terms can be estimated to be equal to one. This can be seen from Equation 4.4, where the ratio between the efficiency of two states are given as

$$\frac{\epsilon_{3.20}}{\epsilon_{3.21}} \approx 1. \tag{4.7}$$

These two efficiency values should be nearly identical, which means that approximating this ratio to be equal to one is a good estimate.

In this thesis a single average value for the efficiency of all detectors of OSCAR is estimated at each required energy. To estimate the error in this method an investigation of the difference in efficiency in each detector was conducted. This was done by using the $LaBr_3$-detectors as signal triggers for the data, to investigate the angular distribution of the chosen gamma ray transition as well as the efficiency of each detector in OSCAR. The 4.44 MeV gamma ray from the 4.44 MeV $2^+$ state in $^{12}$C is an E2-transition and has an angular distribution which is not isotropic. The resulting angular distribution is shown in the upper figure of Figure 4.13, where the measurements are plotted together with a previous measurement of the angular distribution of this gamma ray transition using the $^{12}C(p, p')$-reaction with a beam energy of 10.5 MeV, performed by T. K. Eriksen[44]. In the bottom panel of Figure 4.13 a

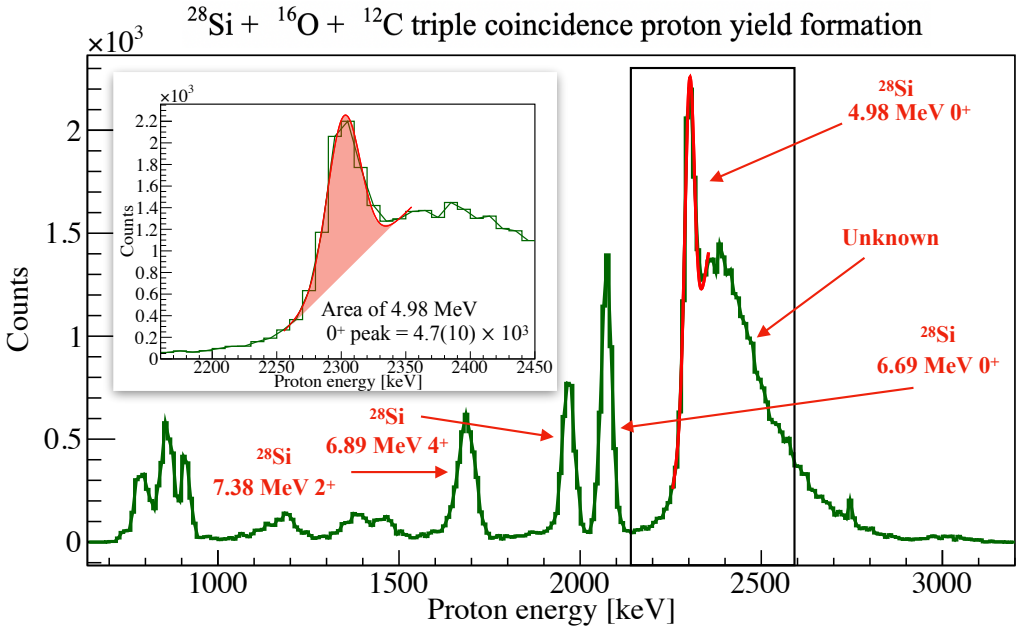


**Figure 4.11:** Triple-coincidence yield proton spectra from $^{28}$Si data gated on coincidences in Figure 4.10. The area around the 4.98 MeV $0^+$ state is marked and magnified to show which peak is included in the calculation of the proton-gamma-gamma coincidence yield, the red shaded area shows the area of the fit. The area from this sorting will be used in Equation 4.4.

normalisation of the signals from the detectors of OSCAR has been calculated with an error band. From the error band in Figure 4.13 an uncertainty of

$$\Delta\epsilon = \pm 3.8\% \tag{4.8}$$

is calculated using the quadratic error[45](root-mean-square) of the normalised points. This uncertainty will be used for all estimated values for the absolute photo peak efficiency. In principle one could weigh the probability of each detector of OSCAR to detect a gamma ray of 4.44 MeV at a specific angle with the angular distribution presented in Figure 4.13 to obtain the $\Delta\epsilon_{4.44}$ of each detector. This $\Delta\epsilon_{4.44}$ could be used to adjust the efficiency of each detector in OSCAR, making the measured efficiency more precise. This was not done due to time restrictions during this thesis.

The absolute photopeak efficiency was measured using two different methods, yielding three different sets of results as shown in Table 4.2. There is a relatively good agreement between the three different sets of results, except for the absolute photopeak efficiency at 3.20 MeV using the data obtained during this thesis (column containing $E_p = 10.7$ MeV). This efficiency was measured using the 4.98 MeV $0^+$ state in $^{28}$Si. The results using the measured efficiency curve shown in Figure 4.12 and the measured value at $E_p = 16.0$ MeV in Table 4.2 are in good agreement. The reason

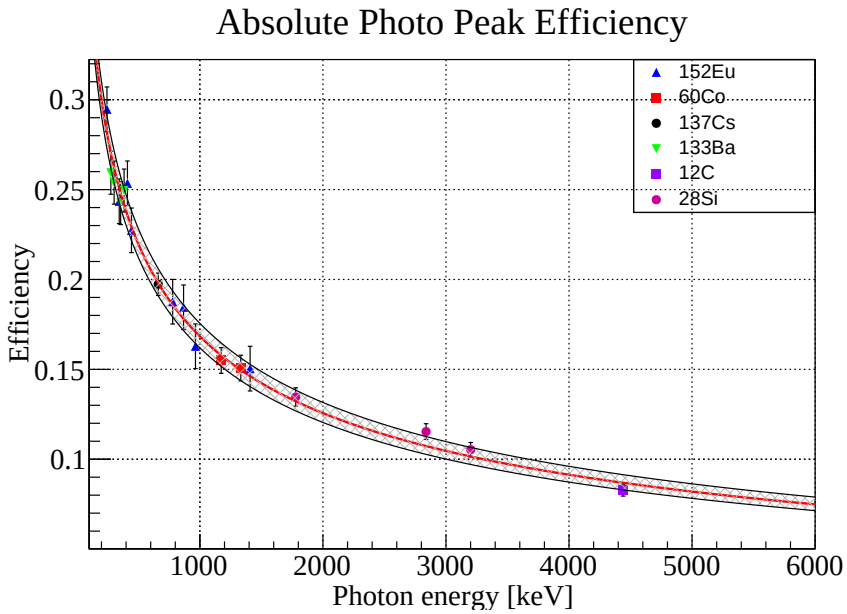


**Figure 4.12:** Graph showing the measured absolute photopeak efficiency curve of OSCAR made by F. Bello[43], included are the measured absolute photopeak efficiency values from the column 'Measured $(p, p')$ at $E_p = 16.0$ MeV' in Table 4.2. The points from Table 4.2 are not included in the fit.

is most likely that using data from an experiment where the protons were energetic enough to be detected in both layers of the particle telescope SiRi made it easier to gate on different states as well as remove background, as discussed in section 2.8. Either way the results shows that the method of using states with gamma decay branching ratio nearly equal to one gives a good estimate of the absolute photopeak efficiency. The challenging part of this method is to estimate an uncertainty for the efficiency, which was estimated to be $\epsilon_{error} = \pm 3.8\%$ for all values for the absolute photopeak efficiency as shown in Equation 4.8. As this thesis work is based on proton-gamma-gamma coincidences, using a single value to describe the efficiency of all combinations of $LaBr_3$-detectors has the consequence of an increased uncertainty. As shown in Figure 4.13 the detectors of OSCAR have an efficiency which deviate from the measured distribution by $\geq 10\%$, except for a single detector which deviates by 13.5%.

### 4.2.4 Angular distribution for a $0^+ \rightarrow 2^+ \rightarrow 0^+$-transition

The angular correlation correction term for the $0^+ \rightarrow 2^+ \rightarrow 0^+$-transition from the Hoyle state to the ground state in $^{12}C$, as shown in Equation 4.3, will be calculated using an angular distribution made from the data collected during this thesis experiment. The result is compared to an angular distribution for the same $0^+ \rightarrow 2^+ \rightarrow 0^+$-transition done by B.M. Alshahrani[34] using the previous scintillator array stationed

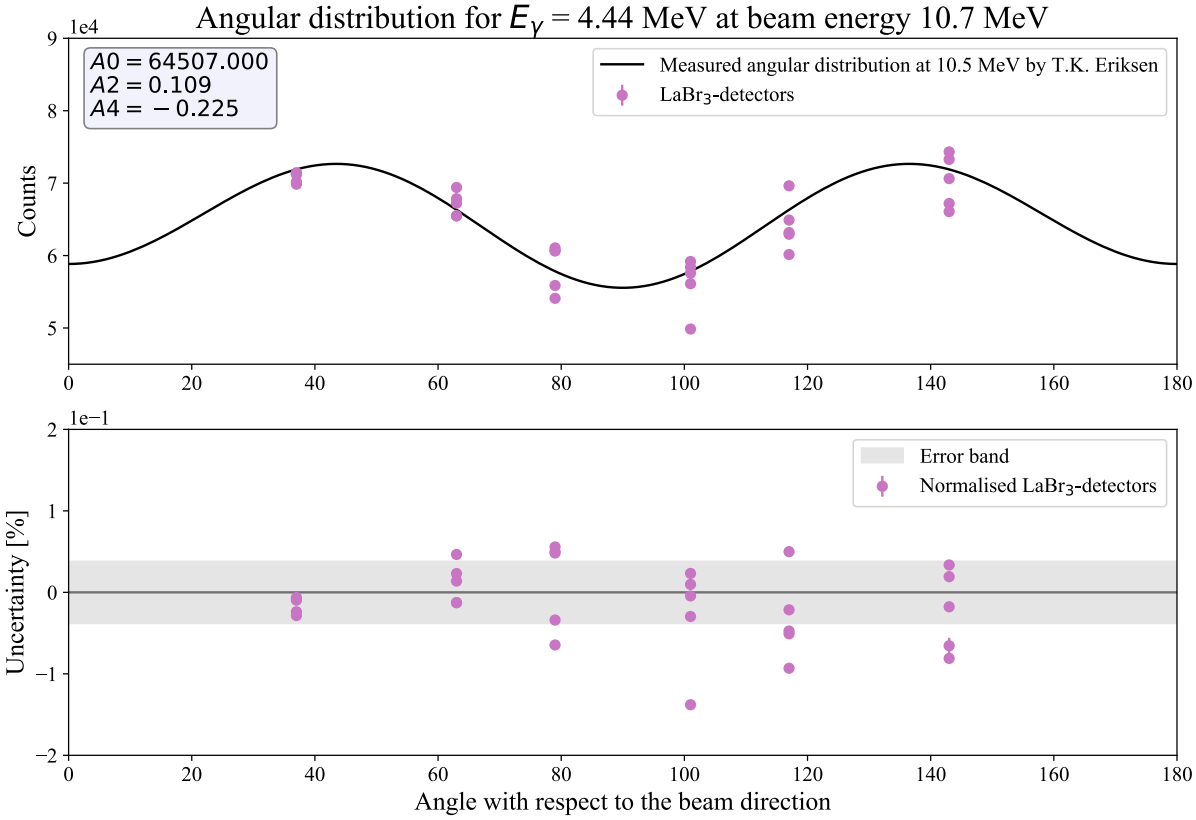


**Figure 4.13:** Top: Graph showing the signals from the 4.44 MeV $2^+$ state in $^{12}$C using all detectors of OSCAR and a measurement of the angular distribution of this state from T. K. Eriksen[44]. Bottom: The signal from each detector in OSCAR is normalised to the angular distribution from T. K. Eriksen[44]. An error band calculated from the quadratic error or root-mean-square of the normalised points is drawn to estimate the error $\Delta\epsilon$ in the efficiency, as seen in Equation 4.8.

at OCL, named CACTUS. CACTUS had a $> 50\%$ of $4\pi$ angle coverage, while the angle coverage of OSCAR is 57% of $4\pi$[31], making it possible to use this angular distribution as a comparison to the current data. The angular correlation distribution for the $0^+ \rightarrow 2^+ \rightarrow 0^+$-transition from the Hoyle state in $^{12}$C calculated using the data collected during this thesis is presented in Figure 4.14. In the upper figure the theoretical and experimental distribution made by B.M. Alshahrani[34] are also shown as a comparison. In the bottom panel the normalised proton-gamma-gamma coincidences are shown, together with an error band where the uncertainty is calculated using the quadratic error[45] (root-mean-square) of the normalised points, showing an error band of $\Delta W_{020}^{7.65}(\theta) \approx \pm 19\%$. The uncertainty which is used in the calculation of the gamma decay branching ratio of the Hoyle state in chapter 5 is the uncertainty at each point of the experimental values of $W_{020}^{7.65}(\theta)$.

To calculate this angular correlation distribution the proton-gamma-gamma co-

| Term | Extrapolated efficiency | Measured $(p, p')$ at $E_p = 10.7$ MeV | Measured $(p, p')$ at $E_p = 16.0$ MeV |
|---|---|---|---|
| $\epsilon_{1.78}$ | 0.1323(4) | 0.126(4) | 0.134(5) |
| $\epsilon_{3.20} \approx \epsilon_{3.21}$ | 0.101(4) | 0.0112(4) | 0.105(4) |
| $\epsilon_{4.44}$ | 0.0869(4) | 0.075(2) | 0.082(3) |

**Table 4.2:** Table showing the results for the three different calculations of the absolute photopeak efficiency for several different energies. The column 'Extrapolated efficiency' is calculated using measurement from OSCAR made by F. Bello[43].

incidences must be sorted by the two OSCAR detector identifications and the angle between them. There are in total 30 $LaBr_3$-detectors used in OSCAR, totaling 435 different detector combinations with approximately 11 different angles between the detector pairs as seen in Table 4.3. Since the analysis consists of proton-gamma-gamma coincidences the events are required to have a single gamma in the energy range of the 3.21 MeV gamma ray, a single gamma in the energy range of the 4.44 MeV gamma ray from the gamma cascade originating from the Hoyle state and a proton populating the Hoyle state. These events were then sorted so that all events sharing the same approximate angle between two detectors were stored in the same spectra. The angular correlation coefficient was calculated at a total of eleven different angles, as seen in Table 4.4, where the symmetrical angles of $\theta$ were combined to increase the statistics at each angle. The experimental $W_{020}^{7.65}(\theta)$ presented in Table 4.4 was used to calculate the results presented in chapter 5.

When calculating the gamma decay branching ratio using the 4.98 MeV $0^+$ state in $^{28}$Si as presented in Equation 4.4, the dependence on the angular correlation correction is removed. The gamma decay branching ratio of this state is also a $0^+ \rightarrow 2^+ \rightarrow 0^+$ transition, making it equal to the angular correlation correction term for the cascade from the Hoyle state. The term in Equation 4.4 is given and estimated as

$$\frac{W_{020}^{4.98}}{W_{020}^{7.65}} \approx 1. \tag{4.9}$$

The angular distribution for the $0^+ \rightarrow 2^+ \rightarrow 0^+$-transition presented in Figure 4.14 fits well with the theoretical and experimental angular distribution made by B.M. Alshahrani[34], except for the region around 180° where there is a clearly

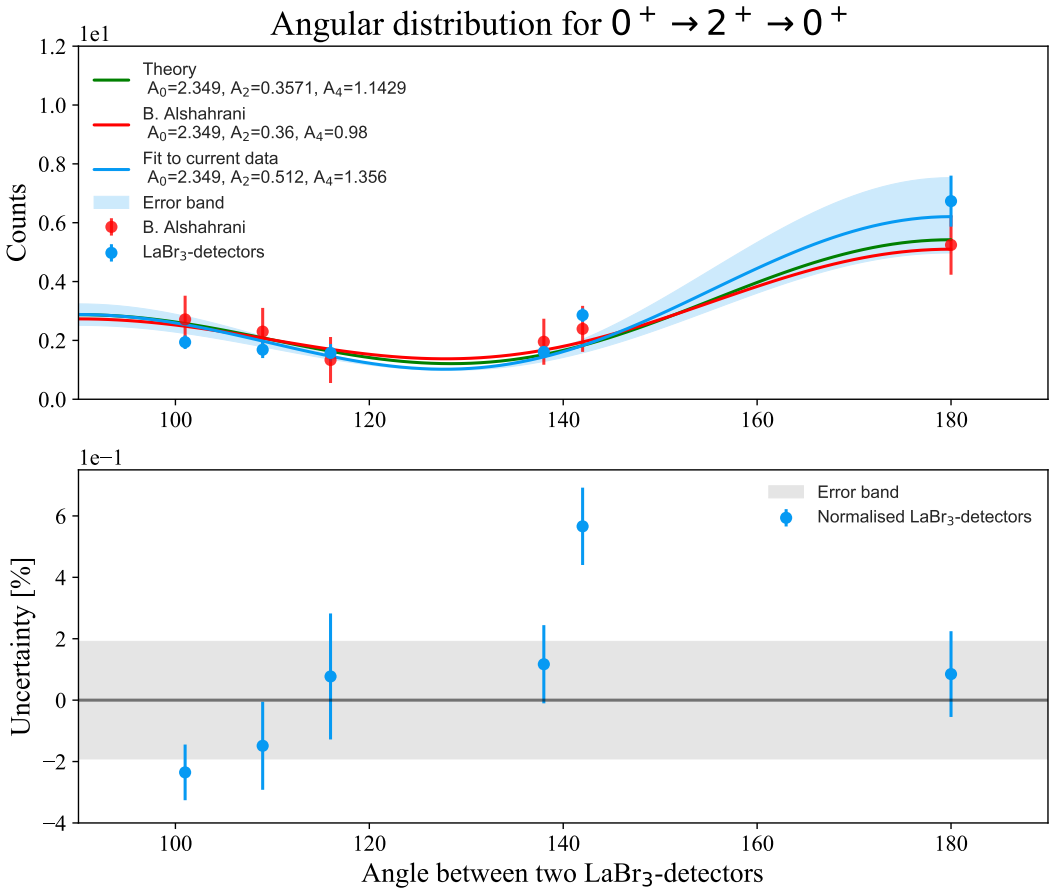


**Figure 4.14:** Upper figure: Graph showing the resulting experimental angular distribution and fit for a $0^+ \rightarrow 2^+ \rightarrow 0^+$-transition calculated from the data collected for this thesis. The theoretical angular distribution and the distribution made by B.M. Alshahrani[34] are also present in the same figure. Bottom figure: The proton-gamma-gamma coincidences are normalised to the fit of the angular distribution. An error band calculated from the quadratic error is fitted to the normalised points.

an increase in the slope for the angular distribution from this thesis. The measured angular distribution at the 180° has the largest uncertainty, similarly to the experimental distribution from B.M. Alshahrani[34]. The uncertainty at all experimental points are from a Gaussian fit to the data sorted for the specific angle, the calculation of this uncertainty can be seen in Appendix A.1.1. The measurement at 142° is an outlier compared to the rest of the angles, this is clearly visible in the bottom panel of Figure 4.14, where it is almost 60% larger than the mathematical fit to the experimental data. The experimental point at 142° from B.M. Alshahrani[34] is also

| $\theta$ [°] | Number of combinations | $\theta$ [°] | Number of combinations |
|---|---|---|---|
| 37.0 | 50 | 101.0 | 50 |
| 42.0 | 30 | 109.0 | 60 |
| 64.0 | 20 | 116.0 | 20 |
| 71.0 | 60 | 138.0 | 30 |
| 79.0 | 50 | 142.0 | 50 |
| | | 180.0 | 15 |

**Table 4.3:** Table showing the approximated angles $\theta$ between two detectors of OSCAR as well as the number of detector combinations for each angle. These values correspond to the term $C_\theta$ in Equation 4.3 as described in section 2.6.

larger than the fit to the data and the theoretical angular distribution, however, the experimental value from this thesis is much higher. The reason for this is not yet understood.

The opposite trend can be seen in the points at 101°, where the data is at a 20% lower value than the fit to the data. The experimental points in Figure 4.14 are calculated from Gaussian fits of spectra containing proton-gamma-gamma coincidences for each angle. As mentioned in section 2.6 the deciding factor of the angular correlation distribution is the amount of statistics. Some peaks in the proton-gamma-gamma spectra for each angle were wider than others, making a mathematical fit quite difficult.

| $\theta$ [°] | $\theta_{\text{symmetrical}}$ [°] | Experimental $W_{020}^{7.65}(\theta)$ | Theoretical $W_{020}^{7.65}(\theta)$ | B. Alshahrani $W_{020}^{7.65}(\theta)$ |
|---|---|---|---|---|
| 101.0 | 79.0 | 1.10(13) | 1.12 | 1.18(35) |
| 109.0 | 71.0 | 0.85(8) | 0.91 | 1.00(35) |
| 116.0 | 64.0 | 0.63(4) | 0.71 | 0.58(34) |
| 138.0 | 42.0 | 0.62(6) | 0.66 | 0.85(34) |
| 142.0 | 37.0 | 0.79(10) | 0.79 | 1.04(34) |
| 180.0 | | 2.69(53) | 2.36 | 2.28(44) |

**Table 4.4:** Table showing all angles between the detectors of OSCAR and the associated angular correlation correction term for the $0^+ \rightarrow 2^+ \rightarrow 0^+$-transition from this thesis. Most angles were summed together with their symmetrical part to increase statistics, this is possible because the angular distribution function is mirrored around 90°. The angular correlation correction terms from the experimental and theoretical values of the angular distribution presented in Figure 4.14, made by B.M. Alshahrani[34] is also included. For explanations of uncertainty calculations see Appendix A.1.2.

# Chapter 5

# Results and discussion

This chapter will present the final measurements of the gamma decay branching ratio of the Hoyle state as well as the resulting radiative width of the Hoyle state. Following is a discussion about the current results and a comparison to previous results. All calculations of uncertainties are explained in Appendix A.1.

## 5.1 The gamma decay branching ratio of the Hoyle state

As a reminder the gamma decay branching ratio of the Hoyle state in Equation 2.9 and Equation 4.3 was given as

$$\left(\frac{\Gamma_\gamma^{\mathrm{E2}}}{\Gamma}\right)^{7.65} = \left(\sum_{\theta=0}^{180} \frac{N_{020}^{7.65}(\theta)}{C_\theta \times W_{020}^{7.65}(\theta)}\right) \frac{1}{K} \times \frac{1}{N_{\mathrm{singles}}^{7.65} \times \epsilon_{3.21}/M \times \epsilon_{4.44}/M} \tag{5.1}$$

When using the radiative width of the 4.98 MeV $0^+$ state in $^{28}$Si as a method of removing the dependency on the angular correlation correction term, the gamma decay branching ratio of the Hoyle state can be written as seen in Equation 2.12 and Equation 4.4 as

$$\left(\frac{\Gamma_\gamma}{\Gamma}\right)^{7.65} = \frac{N_{020}^{7.65}}{N_{020}^{4.98}} \times \frac{N_{\mathrm{singles}}^{4.98}}{N_{\mathrm{singles}}^{7.65}} \times \frac{\epsilon_{1.78}}{\epsilon_{4.44}} \times \frac{\epsilon_{3.20}}{\epsilon_{3.21}} \times \frac{W_{020}^{4.98}}{W_{020}^{7.65}}. \tag{5.2}$$

The measured yield terms $\left(\sum_{\theta=0}^{180} \frac{N_{020}^{7.65}(\theta)}{C_\theta \times W_{020}^{7.65}(\theta)}\right) \frac{1}{K}$, $N_{020}^{7.65}$, $N_{020}^{4.98}$ and singles terms $N_{\mathrm{singles}}^{7.65}$, $N_{\mathrm{singles}}^{4.98}$ can be seen in Table 5.1. The calculation of uncertainties have been described in detail in Appendix A.1. Combining the results from Table 5.1, Table 4.2 and

Table 4.4 by using Equation 5.1 resulted in a gamma decay branching ratio of

$$\left(\frac{\Gamma_{\gamma}^{\mathrm{E2}}}{\Gamma}\right)^{7.65} = 7.08(85) \times 10^{-4}. \tag{5.3}$$

Calculating the gamma decay branching ratio of the Hoyle state using the 4.98 MeV $0^+$ state in $^{28}$Si, as seen in Equation 5.2 resulted in the value

$$\left(\frac{\Gamma_{\gamma}^{\mathrm{E2}}}{\Gamma}\right)^{7.65} = 8.50(47) \times 10^{-3}. \tag{5.4}$$

We observe that there is a major discrepancy between the gamma decay branching ratio measured using only the Hoyle state of $^{12}$C in Equation 5.3 and the measured value using the gamma decay branching ratio of the 4.98 MeV $0^+$ state in $^{28}$Si in Equation 5.4. The values disagree by nearly a factor two and the result using $^{28}$Si is one magnitude of order larger than all previous measurements of this value[4, 5, 6, 7, 8, 9, 10, 11]. Because of this the result in Equation 5.4 is regarded as being highly unlikely to represent a possible physical value. As the theory states in section 2.7, the two measurements of the gamma decay branching ratio of the Hoyle state should theoretically be nearly the same value, therefore this result was not used for calculating the radiative width of the Hoyle state or the rate of the triple-alpha process.

The origin of this discrepancy is most likely caused by the threshold problems with the particle telescope SiRi, as described in subsection 3.3.2. Events registered as having a signal which is beneath the threshold of the E-detector are assumed to deposit energy only in the front layer, or $\Delta$E-layer, of SiRi. If the signal is registered at the threshold limit, some of these signals will be registered in the E-layer and others in the $\Delta$E-layer of SiRi. As the E-detector could not be used in the analysis of this thesis due to the threshold issue, events containing proton-gamma-gamma coincidences could be lost. Another problem is the gain of events regarded as background events because the data analysis had to be done using the $\Delta$E-layer of SiRi, yielding particle spectra where background could not be subtracted. The problem is therefore suspected to be in the ratio between the yield protons and singles protons populating the 4.98 MeV $0^+$ state in $^{28}$Si. This is the same state which is used in the measurement of the absolute photopeak efficiency at 3.20 MeV in subsection 4.2.3, which yielded a result which is highly unlikely to represent a possible value for this efficiency of OSCAR at this energy. It is likely that the same problem is occurring in the calculation determining the gamma decay branching ratio of the Hoyle state using this 4.98 MeV $0^+$ state in $^{28}$Si.

Another possible origin of this discrepancy is the broad peak observed in the proton-gamma-gamma yield spectra in Figure 4.11. The origin of this peak is not understood but suspected to originate from aluminum or possibly from the silicon

| Term | Value |
|---|---|
| $\sum_{\theta=0}^{180} \frac{N_{020}^{7.65}(\theta)}{C_\theta \times W_{020}^{7.65}(\theta)}$ | 14.05(11) |
| $N_{020}^{7.65}$ | 1093.55(7) |
| $N_{020}^{4.98}$ | $4.70(10) \times 10^3$ |
| $N_{\text{singles}}^{7.65}$ | $3.4399(2) \times 10^8$ |
| $N_{\text{singles}}^{4.98}$ | $7.6949(3) \times 10^6$ |

**Table 5.1:** Table showing the calculated terms representing the yields and singles of the 7.65 MeV $0^+$ Hoyle state in $^{12}$C and the 4.98 MeV $0^+$ state in $^{28}$Si from Equation 5.1 and Equation 5.2. See Appendix A.1.3 for explanations of uncertainty calculations.

of SiRi[2] itself. This peak should be present in the spectra for the singles protons populating the 4.98 MeV state in Figure 4.6, however no such broad peak is visible. This could mean that the peak is in the background of the singles spectra and is thus only disturbing the spectra containing the proton-gamma-gamma coincidence yield in Figure 4.11, decreasing the value of $N_{020}^{4.98}$ in Equation 5.2.

The presence of aluminum is evident in the gamma-gamma matrices as seen in Figure 4.3 and Figure 4.4, where several strong peaks are observed. It is also probable that the large amount of background present in the particle spectra for $^{28}$Si as seen in Figure 3.10 are signals from aluminum. Kinematics calculations using Qkinz[41] show that $^{27}$Al has a high abundance of possibly populated states in the energy region of the 4.62 MeV $0^+$ and the 4.89 MeV $0^+$ states in $^{28}$Si. The presence of signals from these states in $^{27}$Al can disturb the particle spectra, especially in the front $\Delta$E-layer where background cannot be subtracted.

The resulting gamma decay branching ratio presented in Equation 5.3 has an uncertainty which is quite large. The source of this uncertainty is in the value of the angular correlation correction term $W_{\theta_k}^{7.65}$ in Equation 5.1 as well as the efficiency terms $\epsilon_{3.21}$ and $\epsilon_{4.44}$. These values are the largest quantitative source of uncertainty in this thesis work. This uncertainty is also affecting the uncertainty of the radiative gamma branching ratio in Equation 5.7 and the radiative width of the Hoyle state in Equation 5.8, making these uncertainties much larger than previous measurements. How these uncertainties were calculated is described in Appendix A.1 and discussed in the next sections.

The reason that the angular correlation distribution is the biggest contributor for

this is that the uncertainty is large at each point of the measured angular correction correlation term $W_{020}^{7.65}(\theta)$(See Appendix A.1.2 for calculation of this uncertainty). The measurement of the gamma decay branching ratio using the method of incorporating the gamma decay branching ratio of the 4.98 Mev $0^+$ state in $^{12}$C would remove this source of uncertainty entirely. Unfortunately this measurement did not yield a good measurement using this method, as seen in Equation 5.4 and discussed previously in this chapter.

## 5.2 The radiative width of the Hoyle state

The radiative width of the Hoyle state can then be calculated using Equation 5.3 and the equation presented in Equation 2.7 given as

$$\frac{\Gamma_{rad}}{\Gamma} = \frac{\Gamma_{\gamma}^{\mathrm{E2}} \times (1 + \alpha_{tot})}{\Gamma} + \frac{\Gamma_{\pi}^{\mathrm{E0}}}{\Gamma}, \tag{5.5}$$

where $\alpha_{tot} = 8.77 \times 10^{-4}$[32] is the theoretical total E2 conversion coefficient. The radiative width of the Hoyle state as seen in Equation 2.6 is given as

$$\Gamma_{rad} = \left[\frac{\Gamma_{rad}}{\Gamma}\right] \times \left[\frac{\Gamma}{\Gamma_{\pi}^{\mathrm{E0}}}\right] \times \left[\Gamma_{\pi}^{\mathrm{E0}}\right]. \tag{5.6}$$

In both Equation 5.5 and Equation 5.6 the terms describing the pair decay from the Hoyle state are the pair decay branching ratio $\Gamma_{\pi}^{\mathrm{E0}}/\Gamma$ as well as the width of pair decay $\Gamma_{\pi}^{\mathrm{E0}}$. The values for these terms were chosen to be identical to the values in the measurement performed by T. Kibédi *et al.*[11]. This follows the recommendation by Freer and Fynbo[3] and it is also the reasonable choice because the result of this thesis will be compared to the results of T. Kibédi *et al.* The values are therefore chosen to be $\Gamma_{\pi}^{\mathrm{E0}} = 62.3(20)$ $\mu$eV[3] for the absolute value of the E0-transition and $\Gamma_{\pi}^{\mathrm{E0}}/\Gamma = 6.72(60) \times 10^{-6}$[3] for the pair decay branching ratio. Inserting these values as well as the result of the gamma decay branching ratio from Equation 5.3 the radiative branching ratio of the Hoyle state becomes

$$\frac{\Gamma_{rad}}{\Gamma} = 7.1(10) \times 10^{-4}. \tag{5.7}$$

Inserting this result as well as previously described values into Equation 2.6, the resulting radiative width of the Hoyle state is then

$$\Gamma_{rad} = 6.6(6) \times 10^{-3} \text{ eV}. \tag{5.8}$$

## 5.3 Comparison to previous measurements

We observe that the value of the radiative branching ratio of the Hoyle state in this thesis is 72% larger than the adopted value at $\Gamma_{rad}/\Gamma = 4.13(11) \times 10^{-4}$ from eight previous measurements presented in Figure 5.1[4, 5, 6, 7, 8, 9, 10, 11]. The result is also consistent with the recently measured value of $\Gamma_{rad}/\Gamma = 6.9(6) \times 10^{-4}$ from T. Kibédi *et al.*[11] as seen in Figure 5.1. The amount of proton-gamma-gamma coincidences were $N_{020}^{7.65} = 1093.55(7)$ which is 5 times larger than the amount of proton-gamma-gamma coincidences obtained using CACTUS in the measurement performed by T. Kibédi *et al.*[11](when the proton-gamma-gamma coincidences are not corrected for the angular correlation). This is a testament as to how efficient OSCAR is compared to CACTUS, where OSCAR consists of 30 $LaBr_3$-detectors and CACTUS consisted of 28 NaI-detectors. There is also a significantly large uncertainty in the current measurement compared to previous measurements, which is discussed in section 5.1.

The result from this thesis was obtained using OSCAR, the new scintillation array consisting of 30 $LaBr_3$-detectors. The measurement performed by T. Kibédi *et al.*[11] used the scintillation array CACTUS, consisting of 28 Nai-detectors. This means that there are now two measurements performed with different scientific equipment supporting this raised value for the radiative branching ratio of the Hoyle state. The fact that this thesis supports the measurement of T. Kibédi *et al.*[11] suggests that further investigation into this measurement is needed. Such a drastic increase in the radiative branching ratio of the Hoyle state compared to the previously adopted value increases the radiative width of the Hoyle state by 73% compared to the previously adopted value of $\Gamma_{rad} = 3.82(37) \times 10^{-3}$ calculated using the adopted value for the radiative branching ratio as presented in Figure 2.3. As the triple-alpha process of the Hoyle state is what is called a 'bottle-neck' process, a change in a value related to this process has the potential to affect nucleosynthesis processes succeeding the triple-alpha process. A direct consequence of this is a reduction in the period of time the star is in the phase of helium-burning, effectively reducing the life-time of the star itself. The raised value will also have an impact on models for stellar evolution and nucleosynthesis processes. An investigation into the effects of this raised value for the triple-alpha process would be highly interesting to study further.

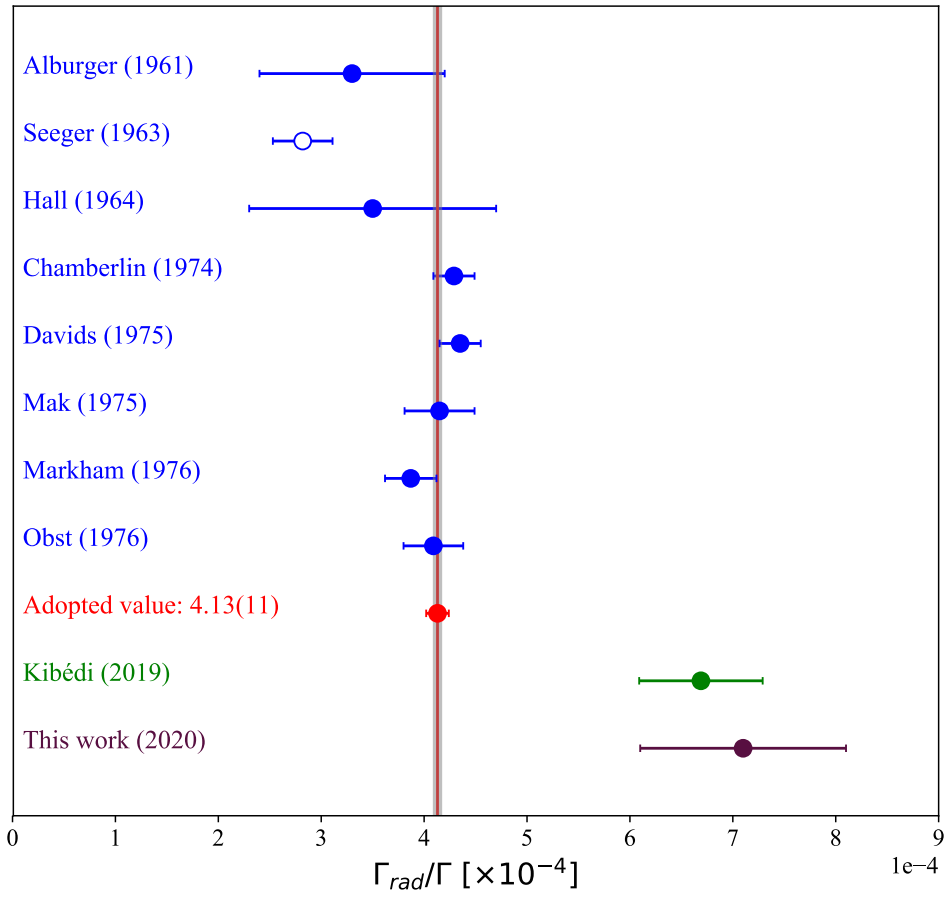


**Figure 5.1:** Figure showing the measurement from this thesis as shown in Equation 5.3 compared to all previous measurements of the ratio between the radiative width and the total width of the Hoyle state. Literature data from Alburger(1961)[4] , Seeger(1963)[33] which is omitted from the adopted value, Hall(1964)[5], Chamberlin(1974)[6], Davids(1975)[7], Mak(1975)[8], Markham(1976)[9] and Obst(1976)[10]. Kibédi(2019)[11] is also omitted from the adopted value due to the gap of time between Obst (1976)[10] and Kibédi (2019)[11]. Figure is originally from Kibédi (2019)[11] and has been modified with permission.

# Chapter 6

# Summary

In this thesis the gamma decay branching ratio of the Hoyle state in $^{12}$C has been measured experimentally using proton-gamma-gamma coincidences. The aim was to perform a measurement using modern equipment and technology and compare the results with previous measurements, where the newest measurement is in disagreement with previous measurements. The previous measurements that were of interest was the adopted value from several experiments performed between 1961 and 1976[4, 5, 6, 7, 8, 9, 10] at $\Gamma_\gamma/\Gamma = 4.13(11) \times 10^{-4}$[11] as well as the newer measurement performed in 2014 by Kibédi *et al.*[11] which yielded a value 68% higher than the previous adopted value at $\Gamma_\gamma/\Gamma = 6.9(6) \times 10^{-4}$[11].

The Hoyle state was populated through a $^{12}\mathrm{C}(p, p'\gamma\gamma)$-reaction with a beam energy of 10.7 MeV at the Oslo Cyclotron Laboratory in January and February 2019 using the $LaBr_3$ array OSCAR and the silicon strip-detector SiRi. Events were defined as the detection of protons, such that a successful event was the detection of a proton populating the Hoyle state in coincidence with two gamma rays of energy 3.21 MeV and 4.44 MeV deexciting from the Hoyle state. The data analysis consisted of two separate methods of analysis, focused on proton-gamma-gamma coincidences using OSCAR and gating on energy in the front layer of SiRi. The first method was to calculate the gamma decay branching ratio of the Hoyle state directly using a ratio between the proton-gamma-gamma coincidences and the total amount of protons populating the Hoyle state, with corrections including the angular distribution of the gamma cascade and the absolute photopeak efficiency of OSCAR itself. The second method consisted of using the gamma decay branching ratio a 4.98 MeV $0^+$ state in $^{28}$Si, having identical value for the first gamma ray in the gamma cascade and equal angular distribution transition as the branching ratio for the Hoyle state. Combining these equations removes the dependency on the angular correlation correction term without impacting the outcome of the calculation.

The measurement resulted in a radiative branching ratio of $\Gamma_\gamma^{\mathrm{E2}}/\Gamma = 7.1(10) \times 10^{-4}$, which is 72% larger than the adopted value from measurements performed between 1961 and 1976[4, 5, 6, 7, 8, 9, 10] and is consistent with the newly obtained

measurement from Kibédi *et al.*[11]. The method using the 4.98 MeV $0^+$ state in $^{28}$Si resulted in a gamma decay branching ratio of $\Gamma_\gamma^{E2}/\Gamma = 8.50(47) \times 10^{-3}$ and was regarded as being an unphysical value which were not used to calculate other properties of the Hoyle state. The radiative width resulted in a value $\Gamma_{rad} = 6.6(6) \times 10^{-3}$ eV which is 73% larger than the value calculated using the previously adopted value for the radiative branching ratio. A method to estimate the absolute photopeak efficiency of OSCAR was tested during this thesis, where states in $^{12}$C and $^{28}$Si with gamma decay branching ratio nearly equal to one was used. The efficiency was estimated using the ratio between protons populating a state yielding a specific gamma ray energy, and the protons populating the state itself. The method yielded results which were in agreement with previous measurements of the absolute photopeak efficiency of OSCAR and was used as an alternative to source measurements. An angular distribution for the $0^+ \rightarrow 2^+ \rightarrow 0^+$-transition from the Hoyle state was calculated, resulting in an angular distribution which agrees with a theoretical and previously measured distribution by B. M. Alshahrani[34] for most angles.

The result of this thesis supports the measurement performed by Kibédi *et al.*[11]. This is therefore the second measurement supporting a raised value for the gamma decay branching ratio of the Hoyle state. The Hoyle state and the triple-alpha process is a 'bottle-neck' process, meaning that an adjustment in the rate of this process can have consequences for several succeeding nucleosynthesis processes. The raised value will have an impact on models of stellar evolution and nucleosynthesis, as well as directly affect the life-time of stars, effectively reducing the period of time the star is in the helium-burning phase.

# Chapter 7

# Future outlook

The motivation for the present work was to perform a measurement of the gamma decay branching ratio of the Hoyle state using newer and more modern technology and compare the result to previous measurements. This was successfully performed and the results suggest that further investigation into this gamma decay branching ratio is needed. Therefore a new measurement of the gamma decay branching width of the Hoyle state was planned during the final analysis of this thesis. Problems and new ideas being discussed during the analysis of the data have been taken into account during the planning, as well as optimization for the use of OCL, SiRi[2] and OSCAR.

The largest difference is the beam energy which will be raised from 10.7 MeV to 16 MeV. A test run has been performed to check that the Hoyle state is reasonably populated at this beam energy. This means that the protons emitted from the Hoyle state will be recorded in both layers of the particle telescope SiRi, making it easier to remove background in the particle spectra, both in time and energy. Another important factor is the use of a tantalum frame to mount the Carbon-12 target, essentially removing the aluminum-background from the gamma ray spectra from OSCAR. The target will consist of Carbon-12 and Silicon-28. A source measurement to measure the efficiency of the absolute photopeak efficiency for gamma rays of energy 3.21 MeV and 4.44 MeV will be done using $^{56}$Co. Doing a source measurement will reduce the uncertainty in the efficiency, which was one of the largest sources of uncertainty in this measurement. The equipment that was damaged or problematic during the experiment of this thesis will be fixed or changed. This includes experimental challenges caused by detectors being wrongly adjusted, which in itself would solve problems such as the missing connection in one of the E-detectors of SiRi. The settings of the SiRi-detector would also be adjusted to detect particle energies appropriate for the protons emitted from the Hoyle state. The aim of this new experiment will be to measure the gamma decay branching ratio for the Hoyle state in $^{12}$C directly and with the use of $^{28}$Si to simplify correction terms, hopefully yielding similar results. Another goal is to do a angular correlation calculation of the $0^+ \rightarrow 2^+ \rightarrow 0^+$ gamma cascade from the Hoyle state to the ground state in $^{12}$C using signals from the $LaBr_3$-detectors

themselves, this requires enormous amounts of statistics.

If the results from this planned measurement supports the findings of the present work and the measurement by T. Kibédi *et al.*[11] it would be interesting to further investigate the consequences of this raised value in stellar models. It is already known that an increased value for the radiative width of the Hoyle state will lead to an increased rate of triple-alpha production yielding $^{12}$C, thus shortening the life-time of stars[11]. Studying this through stellar models will give an estimate as to how much this will impact the stars life-time as well as how this will impact the later nucleosynthesis production paths such as the production of $^{16}$O and $^{20}$Ne, the next bottle-neck processes in the nucleosynthesis of stars.

The measurement performed by T. Kibédi *et al.*[11] and the measurement obtained in this thesis show how improvement of equipment can shed a new light on physical phenomenon such as the Hoyle state, which has been vigorously studied over many years. The results from this thesis support an exciting oddity in the field of nuclear physics and shows that the accurate determination of the triple-alpha rate remains a challenge in the research of low energy nuclear physics.

# Appendices

# Appendix A

# Data analysis

## A.1 Calculation of uncertainty

### A.1.1 Uncertainty of a Gaussian function

A Gaussian function can be expressed as

$$f(x) = P_0 \exp\left[-\frac{1}{2}\left(\frac{x - P_1}{P_2}\right)^2\right] \tag{A.1}$$

where $P_0$, $P_1$ are real constants and $P_2$ is real and non-zero. The constant $P_2$ can be expressed as

$$P_2 = \frac{FWHM}{2\sqrt{2\log 2}} \tag{A.2}$$

where $FWHM$ is the full-width half maximum of the peak of the Gaussian function. The area of a Gaussian function can be written on the form

$$A = P_0 P_2 \sqrt{2\pi}. \tag{A.3}$$

The uncertainty of Equation A.3 can be calculated using the following equation for an uncertainty between a relation $Z = AB$ or $Z = A/B$[45]:

$$\left(\frac{\Delta Z}{Z}\right)^2 = \left(\frac{\Delta A}{A}\right)^2 + \left(\frac{\Delta B}{B}\right)^2. \tag{A.4}$$

Inserting for the uncertainties of each parameter $\Delta P_0$ and $\Delta P_2$ the uncertainty of the area of a Gaussian function becomes

$$\Delta A = \sqrt{\left(\frac{\Delta P_0}{P_0}\right)^2 + \left(\frac{\Delta P_2}{P_2}\right)^2} \times A. \tag{A.5}$$

### A.1.2 Uncertainty of the angular distribution for a $0^+ \rightarrow 2^+ \rightarrow 0^+$-transition

The angular distribution for a $0^+ \rightarrow 2^+ \rightarrow 0^+$-transition is calculated and included in the gamma decay branching ratio as the term $W_{\theta_k}^{7.65}$ in Equation 2.9 (Also seen in Equation 4.3 and Equation 5.1). This term has different values for different angles $\theta_k$ between detectors, where each value has an uncertainty. By calculating the uncertainty using the error band as presented in the upper half of Figure 4.14 at each angle we can calculate the total uncertainty. The equation used for calculating the uncertainty for a relation $Z = A + B$[45] is

$$(\Delta Z)^2 = (\Delta A)^2 + (\Delta B)^2. \tag{A.6}$$

Using the angles as presented in Table 4.4 we have the equation

$$\Delta W_{020}^{7.65} = \pm\Big\{(\Delta W_{101.0}^{7.65})^2 + (\Delta W_{109.0}^{7.65})^2 + (\Delta W_{116.0}^{7.65})^2 + (\Delta W_{138.0}^{7.65})^2 \tag{A.7}$$

$$+ (\Delta W_{142.0}^{7.65})^2 + (\Delta W_{180.0}^{7.65})^2\Big\}^{1/2}. \tag{A.8}$$

However, in Equation A.11 the uncertainty is needed in the form of

$$\left(\frac{\Delta W_{020}^{7.65}}{W_{020}^{7.65}}\right)^2 = \left(\frac{\Delta W_{101.0}^{7.65}}{W_{101.0}^{7.65}}\right)^2 + \left(\frac{\Delta W_{109.0}^{7.65}}{W_{109.0}^{7.65}}\right)^2 + \left(\frac{\Delta W_{116.0}^{7.65}}{W_{116.0}^{7.65}}\right)^2 + \left(\frac{\Delta W_{138.0}^{7.65}}{W_{138.0}^{7.65}}\right)^2 \tag{A.9}$$

$$+ \left(\frac{\Delta W_{142.0}^{7.65}}{W_{142.0}^{7.65}}\right)^2 + \left(\frac{\Delta W_{180.0}^{7.65}}{W_{180.0}^{7.65}}\right)^2. \tag{A.10}$$

### A.1.3 Uncertainty in the gamma decay branching ratio

The uncertainty in the gamma decay branching ratio as calculated directly using $^{12}$C as seen in Equation 2.9(Also seen in Equation 4.3 and Equation 5.2) can be written by using Equation A.4 as

$$\Delta(\Gamma_\gamma^{\mathrm{E2}}/\Gamma)^{7.65} = \pm\left\{\left(\frac{\Delta N_{020,corr}^{7.65}}{N_{020,corr}^{7.65}}\right)^2 + \left(\frac{\Delta N_{singles}^{7.65}}{N_{singles}^{7.65}}\right)^2 + \left(\frac{\Delta W_{020}^{7.65}}{W_{020}^{7.65}}\right)^2 \right. \tag{A.11}$$

$$\left. + \left(\frac{\Delta\epsilon_{3.21}}{\epsilon_{3.21}}\right)^2 + \left(\frac{\Delta\epsilon_{4.44}}{\epsilon_{4.44}}\right)^2\right\}^{1/2} \times (\Gamma_\gamma^{\mathrm{E2}}/\Gamma)^{7.65}. \tag{A.12}$$

The term $N_{020,corr}^{7.65}$ is the area of the Gaussian fit (see Appendix A.1.1) from the term $\sum_{k=1}^{K} \frac{N_k^{7.65}}{C_k \times W_{\theta_k}^{7.65}}$ in Equation 2.9. The term $(\frac{\Delta W_{020}^{7.65}}{W_{020}^{7.65}})^2$ is calculated in Appendix **??** and

the uncertainty estimate for the absolute photopeak efficiency for the terms $(\frac{\Delta\epsilon_{3.21}}{\epsilon_{3.21}})^2$ and $(\frac{\Delta\epsilon_{4.44}}{\epsilon_{4.44}})^2$ can be seen in Appendix 2.8.

When incorporating the gamma decay branching ratio of 4.98 MeV $0^+$ state in $^{28}$Si into the gamma decay branching ratio of the Hoyle state as seen in Equation 2.12 (also seen in Equation 4.4 and Equation 5.2) the uncertainty can be written as

$$\Delta(\Gamma_\gamma^{\mathrm{E2}}/\Gamma)^{7.65} = \pm\left\{\left(\frac{\Delta N_{020}^{7.65}}{N_{020}^{7.65}}\right)^2 + \left(\frac{\Delta N_{singles}^{7.65}}{N_{singles}^{7.65}}\right)^2 + \left(\frac{\Delta N_{020}^{4.98}}{N_{020}^{4.98}}\right)^2 \right. \tag{A.13}$$

$$\left. + \left(\frac{\Delta N_{singles}^{4.98}}{N_{singles}^{4.98}}\right)^2 + \left(\frac{\Delta\epsilon_{1.78}}{\epsilon_{1.78}}\right)^2 + \left(\frac{\Delta\epsilon_{4.44}}{\epsilon_{4.44}}\right)^2\right\}^{1/2} \times (\Gamma_\gamma^{\mathrm{E2}}/\Gamma)^{7.65}. \tag{A.14}$$

### A.1.4 Uncertainty in the radiative branching ratio and radiative width

The uncertainty in the radiative branching ratio can be calculated by using Equation A.4 such that

$$\left(\frac{\Delta\Gamma_{rad}/\Gamma}{\Gamma_{rad}/\Gamma}\right)^2 = \left(\frac{\Delta(\Gamma_\gamma^{\mathrm{E2}}/\Gamma)^{7.65}}{(\Gamma_\gamma^{\mathrm{E2}}/\Gamma)^{7.65}}\right)^2 + \left(\frac{\Delta\Gamma_\pi^{\mathrm{E0}}/\Gamma}{\Gamma_\pi^{\mathrm{E0}}/\Gamma}\right)^2. \tag{A.15}$$

The uncertainty for the radiative width of the Hoyle state as presented in Equation 5.8 using the calculated uncertainty for the radiative branching ratio Equation A.15 and for a relation $Z = AB$ and $Z = A/B$ in Equation A.4 was calculated using the equation

$$\Delta\Gamma_{rad} = \pm\left\{\left(\frac{\Delta\Gamma_{rad}/\Gamma}{\Gamma_{rad}/\Gamma}\right)^2 + \left(\frac{\Delta\Gamma_\pi^{\mathrm{E0}}/\Gamma}{\Gamma_\pi^{\mathrm{E0}}/\Gamma}\right)^2 + \left(\frac{\Delta\Gamma_\pi^{\mathrm{E0}}}{\Gamma_\pi^{\mathrm{E0}}}\right)^2\right\}^{1/2} \times \Gamma_{rad}. \tag{A.16}$$

# Bibliography


[1] F Hoyle, Mount Wilson, and Palomar Observatories. ON NUCLEAR REACTIONS OCCURRING IN VERY HOT STARS. I. THE SYNTHESIS OF ELEMENTS FROM CARBON TO NICKEL. URL http://articles.adsabs.harvard.edu/pdf/1954ApJS....1..121H.

[2] M. Guttormsen, A. Bürger, T.E. Hansen, and N. Lietaer. The siri particle-telescope system. *Nuclear Instruments and Methods in Physics Research Section A: Accelerators, Spectrometers, Detectors and Associated Equipment*, 648 (1):168 – 173, 2011. ISSN 0168-9002. doi: https://doi.org/10.1016/j.nima.2011.05.055. URL http://www.sciencedirect.com/science/article/pii/S0168900211010205.

[3] M. Freer and H. O.U. Fynbo. The Hoyle state in 12C. *Progress in Particle and Nuclear Physics*, 78:1–23, 2014. ISSN 01466410. doi: 10.1016/j.ppnp.2014.06.001. URL http://dx.doi.org/10.1016/j.ppnp.2014.06.001.

[4] David E. Alburger. Gamma-ray decay of the 7.66-mev level of $^{12}$C. *Phys. Rev.*, 124:193–198, Oct 1961. doi: 10.1103/PhysRev.124.193. URL https://link.aps.org/doi/10.1103/PhysRev.124.193.

[5] I. Hall and N.W. Tanner. The radiative decay of the 7.66 mev level of $^{12}$C. *Nuclear Physics*, 53:673 – 684, 1964. ISSN 0029-5582. doi: https://doi.org/10.1016/0029-5582(64)90646-7. URL http://www.sciencedirect.com/science/article/pii/0029558264906467.

[6] D. Chamberlin, D. Bodansky, W.W. Jacobs, and D.L. Oberg. Electromagnetic decay of the 7.65-MeV state of C-12. *Phys. Rev. C*, 9:69–75, 1974. doi: 10.1103/PhysRevC.9.69.

[7] C. N Davids, R.C Pardo, and A.W Obst. *Phys. Rev. C*, 11, 1975.

[8] H. B. Mak, H. C. Evans, G. T. Ewan, A. B. McDonald, and T. K. Alexander. Radiative decay of the second excited state of $^{12}$C. *Phys. Rev. C*, 12:1158–1166, Oct 1975. doi: 10.1103/PhysRevC.12.1158. URL https://link.aps.org/doi/10.1103/PhysRevC.12.1158.

[9] R.G. Markham, Sam M. Austin, and M.A.M. Shahabuddin. A measurement of rad/ for the 7.654 mev state of 12c and the rate of the stellar 3 reaction. *Nuclear Physics A*, 270(2):489 – 500, 1976. ISSN 0375-9474. doi: https://doi.org/10.1016/0375-9474(76)90458-9. URL http://www.sciencedirect.com/science/article/pii/0375947476904589.

[10] A. W. Obst and W. J. Braithwaite. Measurement of the radiative branching ratio for the 7.65-MeV state in C12 using the cascade gamma decays. *Physical Review C*, 13(5):2033–2043, 1976. ISSN 05562813. doi: 10.1103/PhysRevC.13.2033.

[11] T. Kibédi, B. Alsehany, A.E. Stuchbery, A.C. Larsen, A. Görgen, S. Siem, and M. Guttormsen. The radiative width of the hoyle state from gamma-ray spectroscopy. *Submitted to PRL*, December 2019.

[12] Carl Sagan. Cosmos - episode 1: The shores of the cosmic ocean, 1980.

[13] M. Livio, D. Hollowell, A. Weiss, and J. W. Truran. The anthropic significance of the existence of an excited state of 12C. *Nature*, 340(6231):281–284, 1989. ISSN 00280836. doi: 10.1038/340281a0. URL https://doi.org/10.1038/340281a0.

[14] Fred Hoyle. The Universe : Past and present reflections. *Annual Review of Astronomy and Astrophysics*, 20, 1982. URL https://doi.org/10.1146/annurev.aa.20.090182.000245.

[15] C.E. Rolfs and W.S. Rodney. *Cauldrons in the Cosmos: Nuclear Astrophysics*. Theoretical Astrophysics. University of Chicago Press, 1988. ISBN 9780226724577. URL https://books.google.no/books?id=BHKLFPUS1RcC.

[16] W. A. WENZEL D. N. F. DUNBAR, R. E. PIXLEY and W. WHALING. The 7.68-Mev State in 12C. pages 649–650, 1953. URL https://journals.aps.org/pr/pdf/10.1103/PhysRev.92.649.

[17] Christian Iliadis. *Nuclear physics of stars; 2nd ed.* Wiley, Hoboken, NJ, 2015. doi: 10.1002/9783527692668. URL http://cds.cern.ch/record/2020261.

[18] T. Kajino, W. Aoki, A.B. Balantekin, R. Diehl, M.A. Famiano, and G.J. Mathews. Current status of r-process nucleosynthesis. *Progress in Particle and Nuclear Physics*, 107:109 – 166, 2019. ISSN 0146-6410. doi: https://doi.org/10.1016/j.ppnp.2019.02.008. URL http://www.sciencedirect.com/science/article/pii/S0146641019300201.

[19] Daniel Kasen, Brian Metzger, Jennifer Barnes, Eliot Quataert, and Enrico Ramirez-Ruiz. Origin of the heavy elements in binary neutron-star mergers from a gravitational-wave event. *Nature*, 551, 10 2017. doi: 10.1038/nature24453.

[20] Lei Hu, Xuefeng Wu, Igor Andreoni, Michael C. B. Ashley, Jeff Cooke, Xiangqun Cui, Fujia Du, Zigao Dai, Bozhong Gu, Yi Hu, Haiping Lu, Xiaoyan Li, Zhengyang Li, Ensi Liang, Liangduan Liu, Bin Ma, Zhaohui Shang, Tianrui Sun, N.B. Suntzeff, Charling Tao, Syed A. Uddin, Lifan Wang, Xiaofeng Wang, Haikun Wen, Di Xiao, Jin Xu, Ji Yang, Shihai Yang, Xiangyan Yuan, Hongyan Zhou, Hui Zhang, Jilin Zhou, and Zonghong Zhu. Optical observations of ligo source gw 170817 by the antarctic survey telescopes at dome a, antarctica. *Science Bulletin*, 62(21):1433 – 1438, 2017. ISSN 2095-9273. doi: https://doi.org/10.1016/j.scib.2017.10.006. URL http://www.sciencedirect.com/science/article/pii/S2095927317305224.

[21] F Hoyle. THE SYNTHESIS OF THE ELEMENTS FROM HYDROGEN *. pages 344–383, 1946. URL http://articles.adsabs.harvard.edu/pdf/1946MNRAS.106..343H.

[22] Meng Wang, G. Audi, F. G. Kondev, W.J. Huang, S. Naimi, and Xing Xu. The AME2016 atomic mass evaluation (II). tables, graphs and references. *Chinese Physics C*, 41(3):030003, mar 2017. doi: 10.1088/1674-1137/41/3/030003. URL https://doi.org/10.1088%2F1674-1137%2F41%2F3%2F030003.

[23] E. Margaret Burbidge, G. R. Burbidge, William A. Fowler, and F. Hoyle. Synthesis of the Elements in Stars. *Reviews of Modern Physics*, 29(4):547–650, oct 1957. ISSN 0034-6861. doi: 10.1103/RevModPhys.29.547. URL https://link.aps.org/doi/10.1103/RevModPhys.29.547.

[24] H. A. Bethe. Energy production in stars. *Phys. Rev.*, 55:434–456, Mar 1939. doi: 10.1103/PhysRev.55.434. URL https://link.aps.org/doi/10.1103/PhysRev.55.434.

[25] E.E Salpeter. Nuclear reactions in stars without hydrogen*. *Astrophysical Journal*, 115:326–328, 1952. doi: https://ui.adsabs.harvard.edu/link_gateway/1952ApJ...115..326S/doi:10.1086/145546. URL http://articles.adsabs.harvard.edu/pdf/1952ApJ...115..326S.

[26] Ernst Julius Öpik. Stellar models with variable composition. ii. sequences of models with energy generation proportional to the 15th power of temperature. *Proc. R. Irish Acad*, A54:44–47, 1952.

[27] G. Audi, A.H. Wapstra, and C. Thibault. The ame2003 atomic mass evaluation: (ii). tables, graphs and references. *Nuclear Physics A*, 729(1):337 – 676, 2003. ISSN 0375-9474. doi: https://doi.org/10.1016/j.nuclphysa.2003.11.003. URL http://www.sciencedirect.com/science/article/pii/S0375947403018098. The 2003 NUBASE and Atomic Mass Evaluations.

[28] T. Kibédi, T.W. Burrows, M.B. Trzhaskovskaya, P.M. Davidson, and C.W. Nestor. Evaluation of theoretical conversion coefficients using bricc. *Nuclear Instruments and Methods in Physics Research Section A: Accelerators, Spectrometers, Detectors and Associated Equipment*, 589(2):202 – 229, 2008. ISSN 0168-9002. doi: https://doi.org/10.1016/j.nima.2008.02.051. URL `http://www.sciencedirect.com/science/article/pii/S0168900208002520`.

[29] T. Kibédi, A. E. Stuchbery, G. D. Dracoulis, A. Devlin, A. Teh, and K. Robertson. New approach to determine the radiative width of the hoyle state. *AIP Conference Proceedings*, 1109(1):66–71, 2009. doi: 10.1063/1.3122264. URL `https://aip.scitation.org/doi/abs/10.1063/1.3122264`.

[30] T. K. Eriksen, T. Kibdi, M. W. Reed, A. E. Stuchbery, K. J. Cook, A. Akber, B. Alshahrani, A. A. Avaa, K. Banerjee, A. C. Berriman, L. T. Bezzina, L. Bignell, J. Buete, I. P. Carter, B. J. Coombes, J. T. H. Dowie, M. Dasgupta, L. J. Evitts, A. B. Garnsworthy, M. S. M. Gerathy, T. J. Gray, D. J. Hinde, T. H. Hoang, S. S. Hota, E. Ideguchi, P. Jones, G. J. Lane, B. P. McCormick, A. J. Mitchell, N. Palalani, T. Palazzo, M. Ripper, E. C. Simpson, J. Smallcombe, B. M. A. Swinton-Bland, T. Tanaka, T. G. Tornyi, and M. O. de Vries. Improved precision on the experimental e0 decay branching ratio of the hoyle state, 2020.

[31] F. Zeiser, G.M. Tveten, F.L. Bello Garrote, M. Guttormsen, A.C. Larsen, V.W. Ingeberg, A. Görgen, T. Renstrøm, and S. Siem. The $\gamma$-ray energy response of the oslo scintillator array oscar, 2020. To be published on arXiv 14.08.2020.

[32] Tibor Kibédi and R. H. Spear. Electric monopole transitions between 0+ states for nuclei throughout the periodic table. *Atomic Data and Nuclear Data Tables*, 89(1):77–100, 2005. ISSN 0092640X. doi: 10.1016/j.adt.2004.11.002.

[33] P.A. Seeger and R. W. Kavanagh. *Nucl.Phys*, 46:577, Oct 1963.

[34] Badriah Mohammed Alshahrani. *Measurement of the radiative branching ratio for the Hoyle state using cascade gamma decays*. PhD thesis, Australian National University, 2015.

[35] Fysisk institutt, UiO. The ocl m-35 scanditronix, an overview, 2011. URL `https://www.mn.uio.no/fysikk/forskning/om/infrastruktur/Syklotronlaboratoriet/`. [Online; accessed June 22, 2020].

[36] Fysisk institutt, UiO. Oscar - new generation scintillator detectors for nuclear research in norway, 2017. URL `https://www.mn.uio.no/fysikk/english/research/projects/oscar/`. [Online; accessed July 26, 2020].

[37] AMETEK ORTEC. Lanthanum bromide scintillation radiation detectors, 2020. URL https://www.ortec-online.com/products/radiation-detectors/scintillation-detectors/scintillation-detector-types/lanthanum-bromide-detectors. [Online; accessed August 9, 2020].

[38] Cary N Davids and T.I Bonner. Enhancement of the 3 4He -> 12C Reaction rate by inelastic proton scattering. *The Astrophysical Journal*, 166:405–410, 1971. doi: 10.1086/150968.

[39] J. B. Swint, A. C.L. Barnard, T. B. Clegg, and J. L. Weil. Cross sections as a function of energy for the scattering of protons from 12C. *Nuclear Physics*, 86 (1):119–129, 1966. ISSN 00295582. doi: 10.1016/0029-5582(66)90295-1.

[40] William R Leo. *Techniques for nuclear and particle physics experiments: a how-to approach; 3rd ed.* Springer, Berlin, 1994. doi: 10.1007/978-3-642-57920-2. URL https://cds.cern.ch/record/302344.

[41] V. W. Ingeberg and E. Lima. oslocyclotronlab/qkinz. doi: 10.5281/zenodo.1206099.

[42] Anna Camp, Arturo Vargas, and Jos M. Fernndez-Varea. Determination of labr3(ce) internal background using a hpge detector and monte carlo simulations. *Applied Radiation and Isotopes*, 109:512 – 517, 2016. ISSN 0969-8043. doi: https://doi.org/10.1016/j.apradiso.2015.11.093. URL http://www.sciencedirect.com/science/article/pii/S0969804315303328. Proceedings of the 20th International Conference on Radionuclide Metrology and its Applications 811 June 2015, Vienna, Austria.

[43] Frank G. Bello. personal communication. f.l.b.garrote@mail.uio.no.

[44] Tomas Kvalheim Eriksen. *Investigation of the Hoyle state in 12C and the related triple alpha reaction rate.* PhD thesis, Australian National University, 2018.

[45] G. L. Squires. *Practical physics.* Cambrigde University Press, 2001. ISBN 0521770459.